Crystalline grain engineered $CsPbIBr_2$ films for indoor photovoltaics

Paheli Ghosh[a], Jochen Bruckbauer[b], Carol Trager-Cowan[b] and Lethy Krishnan Jagadamma[a*]

[a]Energy Harvesting Research Group, School of Physics & Astronomy, SUPA, University of St Andrews, St Andrews, KY16 9SS, United Kingdom

[b]Department of Physics, SUPA, University of Strathclyde, Glasgow, G4 0NG, United Kingdom

Email: lkj2@st-andrews.ac.uk

Abstract

Indoor photovoltaic devices have garnered profound research attention in recent years due to their prospects of powering 'smart' electronics for the Internet of Things (IoT). Here it is shown that all-inorganic Cs-based halide perovskites are promising for indoor light harvesting due to their wide bandgap matched to the indoor light spectra. Highly crystalline and compact $CsPbIBr_2$ perovskite based photovoltaic devices have demonstrated a power conversion efficiency (PCE) of 14.1% under indoor illumination of 1000 lux and 5.9% under 1 Sun. This study revealed that a reduction in grain misorientation, as well as suppression of defects in the form of metallic Pb in the perovskite film are crucial for maximising the photovoltaic properties of $CsPbIBr_2$ based devices. It was demonstrated that a pinhole free $CsPbIBr_2$/Spiro-OMeTAD interface preserves the perovskite α phase and enhances the air stability of the $CsPbIBr_2$ devices. These devices, despite being unencapsulated, retained >55% of the maximum PCE even when stored under 30% relative humidity for a shelf-life duration of 40 days and is one of the best stability data reported so far for $CsPbIBr_2$ devices.

Keywords

All-inorganic perovskite, EBSD, grain misorientation, Internet of Things, mixed halides, XPS

1. Introduction

The constant decrease in energy requirements for the Internet of Things (IoT) has resulted in immense research being focussed on self-powered wireless devices. The self-powering feature is expected to circumvent the issues with energy storage and hence, contribute towards the growth and sustainability of IoT technology. Many of these wireless devices are expected to be used indoors, with minimal power requirement in the range of micro to milliwatts and

hence, efficient, and reliable indoor photovoltaics (IPV) would serve as the suitable power source. IPVs suitable for powering the sensors should not only have high power conversion efficiency (PCE) but must also encompass attributes such as low cost, flexibility, robustness and be easily processable from earth-abundant materials. Though commercial crystalline silicon solar cells are suitable for harvesting solar radiation, the relatively narrow bandgap (1.1 eV), complex and energy-intensive fabrication requirements and high trap-assisted recombination under low-intensity illumination limit their application as indoor photovoltaics [1,2]. Hence the development of alternate absorber materials for IPVs is of paramount importance to sustainably support the rapidly growing IoT technology. These absorber materials should have wide bandgap (1.9 eV) and fewer defects since the indoor artificial light sources such as white light emitting diodes (LEDs) and fluorescent lamps (CFLs) primarily emit photons in the visible region (400 - 700 nm) and have lower intensity (0.1 - 1 mW cm^{-2}) compared to the 1 Sun spectrum [3–5].

Hybrid halide perovskite semiconductors are promising for many optoelectronic applications owing to their favourable attributes of high charge carrier mobility, wide absorption spectrum, tunable bandgap, ease of device fabrication using solution-processed and vacuum deposition techniques and have demonstrated outstanding solar cell PCE of 25.5% under 1 Sun [6]. Among them, all inorganic halide perovskites such as $CsPbX_3$ (where X = Cl, Br or I) have a tunable bandgap ranging from 1.73 eV for $CsPbI_3$ to 2.3 eV for $CsPbBr_3$ and possess high thermal stability compared to their organic counterparts [7,8]. However, $CsPbI_3$ suffers from severe phase instability issues as the photo-active perovskite α-phase is only stable at temperatures >330ºC. The $CsPbBr_3$ shows appreciable stability, but the large bandgap (E_g ~ 2.3 eV) does not favour absorption in the visible region, thus, limiting their PV applications. The issues of pristine $CsPbX_3$ perovskites can be overcome by replacing some of the I^- ions with Br^- ions with amenability to tailoring of the bandgap.

$CsPbIBr_2$ with a bandgap of ~2.05 eV [9] is suitable for indoor photovoltaics, integration in tandem devices and smart PV windows [10]. Previously, the application of $CsPbIBr_2$ has been explored in outdoor solar cells (with PCE ranging from 5-10%), photodetectors [11–14], and light emitting diodes [15]. Most of these reported studies on $CsPbIBr_2$ perovskite photovoltaics involved either high temperature annealing (ranging from 200°C - 360°C) of the active layer [16–21] or the charge transporting layers [9,16–18,22–25] or pre-heating the substrate (40 - 80 °C) [19]. This not only makes the fabrication process complex but also incompatible with flexible substrates and wearable technologies which are being widely

explored in the IoT. Moreover, these devices show appreciable hysteresis (ranging from 10 - 50%) and the air stability is often not explored. So far, the photovoltaic research on inorganic Cs-based perovskite solar cells has been primarily optimised for 1 Sun illumination with the application in indoor photovoltaics hardly investigated [26–29]. But the recent explosion in the IoT and indoor photovoltaics has necessitated the development of new semiconducting materials processable at temperatures low enough to be compatible with flexible substrates such as polyethylene terephthalate (PET) to maximise the chances of integration while implementing these devices as indoor light harvesters to power sensors in the IoT applications. *So, the present investigation aims to obtain $CsPbIBr_2$ devices with competitive 1 Sun and indoor light harvesting properties in combination with low hysteresis effects, enhanced ambient stability and feasibility of fabrication at a processing temperature low enough to be compatible with flexible plastic substrates.*

In this study, $CsPbIBr_2$ films with optimised surface features and crystalline properties were developed and the corresponding indoor photovoltaic devices demonstrated a champion PCE of 14% under white LED illumination and good air stability. These devices, without any encapsulation, retained more than 55% of the initial PCE even after 40 days of storage in 30% humidity. Detailed microstructural analysis using X-ray photoemission spectroscopy (XPS) and electron backscattered diffraction (EBSD) revealed that treatment of the perovskite layer using selected anti-solvents is not only effective in achieving the desired morphology but also in reducing the surface defects in the form of metallic Pb and the grain misorientation. The present study demonstrates the promising potential of all-inorganic $CsPbIBr_2$ perovskites for indoor light harvesting and provides *a fresh avenue for research on Cs-based indoor photovoltaic devices.*

2. Methods

(a) Materials

The chemicals used to prepare the $CsPbIBr_2$ perovskite solution [CsI and $PbBr_2$, 99.999% purity] were used as received from Alfa Aesar. The SnO_2 solution (CAS 18282-10-5) for the electron transport layer (ETL) was bought from Alfa Aesar and diluted to the volume ratio 1:6.5 in deionized (DI) water prior to spin coating. The materials used for hole transport layer (HTL) solution preparation [2,2',7,7'-Tetrakis[N,N-di(4-methoxyphenyl)amino]-9,9'-spirobiflourene (Spiro-OMeTAD, >99% purity), 4-tert-butyl pyridine (tBP, 96% purity), lithium-bis(tri-fluoromethanesulfonyl)imide (Li-TFSI, 99.95% purity) and tris(2-(1H-pyrazol-1-yl)-4-tert-butylpyridine)cobalt(III) tri[bis(trifluoromethane)sulfonimide] (FK 209) were

purchased from Ossila, Sigma Aldrich and Greatcellsolar Materials, respectively. Solvents such as dimethyl sulfoxide (DMSO, anhydrous, ≥99.9%), chlorobenzene (anhydrous, 99.8%), acetonitrile (anhydrous, 99.8%), and diethyl ether (anhydrous, ≥99.7%) were purchased from Sigma Aldrich.

(b) Device fabrication

Patterned indium tin oxide (ITO)-coated glass substrates (glass/ITO with a sheet resistance of 15 Ω $\square^{-1}$) were sequentially cleaned with sodium dodecyl sulphate (SDS), deionized water, acetone and isopropyl alcohol followed by plasma cleaning for 3 minutes with oxygen plasma in a Plasma Asher. A compact hole-blocking SnO_2 ETL was spin-coated using 100 µL of SnO_2 solution [diluted to 1:6.5 volume ratio in DI water] at 3000 rpm for 30 seconds, followed by thermal annealing at 150°C for 30 minutes on a hot plate in ambient conditions inside a laminar flow fume hood. For the perovskite solution, CsI (1 M; 259.8 mg) and $PbBr_2$ (1 M; 367.01 mg) as precursor materials were dissolved in anhydrous DMSO (1 mL) and stirred continuously for 2 hours at room temperature to achieve the desired $CsPbIBr_2$ composition. The $CsPbIBr_2$ perovskite solution was spin-coated on top of the SnO_2 ETL using a two-step spin-coating procedure, the first step at 1000 rpm for 15 seconds followed by a second step at 4000 rpm for 45 seconds. 90 µL of the mixed halide perovskite solution was used for spin coating, followed by treatment with 750 µL of different anti-solvents (chlorobenzene and diethyl ether) during the last 15th second of the second spin coating step. These films were then annealed at 150°C on a hot plate for 15 minutes. The films turned brown immediately upon placing them on the hot plate. For the HTL, 65 µL of a Spiro-OMeTAD solution [(72.3 mg of Spiro-OMeTAD, 28.8 µL of tBP, 17.5 µL of a Li-TFSI solution (520 mg Li-TFSI in 1 mL acetonitrile) and 29 µL of a FK-209 solution (300 mg FK-209 in 1 mL acetonitrile)] in 1 mL chlorobenzene was spin coated at 4000 rpm for 30 seconds on the perovskite active layer. Before spin coating, the individual solutions for HTL were thoroughly mixed using the vortex mixer. The perovskite and HTL weighing, precursor solution preparation, stirring, perovskite active layer and HTL spin coating were undertaken in a nitrogen-filled glove box with relative humidity <15%. The glass/ITO/SnO_2/perovskite/Spiro-OMeTAD structures were wrapped in Aluminum foil and left overnight in a desiccator at room temperature for oxygen doping of Spiro-OMeTAD. Finally, a 60 nm thick Au electrode was thermally evaporated (chamber pressure $3x10^{-6}$ mbar) on top of the HTM to complete the perovskite solar cell device. An aperture mask was employed to determine the effective active area of the device as 0.0646 cm^2.

(c) Films for characterization

The $CsPbIBr_2$ films used for UV-Vis absorption spectroscopy, X-ray diffraction (XRD) and scanning electron microscopy (SEM) characterization were prepared on non-patterned ITO substrates (sheet resistance 15 $\Omega\ \square^{-1}$) using the same protocol for the active layer as mentioned earlier. Prior to the perovskite spin coating, the substrates were thoroughly cleaned using the same cleaning procedure as followed during the device fabrication.

(d) Characterization of CsPbIBr2 perovskite films and devices

The UV-Vis absorption spectra of $CsPbIBr_2$ perovskite thin films were recorded using a Cary 300 Bio Spectrometer over the wavelength range 300 – 800 nm.

The XRD patterns of the annealed perovskite films were collected using a Panalytical Empyrean X-ray diffractometer operating in Bragg-Brentano geometry with Cu Kα_1 radiation and an X'celerator RTMS detector. Data were acquired in the range 10° - 60° with a step size of 0.017° and a time per step of 147.955 seconds.

The surface morphology of the perovskite films was studied using a field-emission scanning electron microscope (Hitachi S4800 equipment). Electron backscattered diffraction (EBSD) measurements were performed in a variable pressure field emission gun scanning electron microscope (FEI Quanta 250) using a Nordlys EBSD detector from Oxford Instruments. The EBSD datasets from all samples were acquired at 20 kV and a sample tilt of 70˚ with respect to the normal of the incident electron beam. Data analysis was performed using the freely available Matlab-based toolbox MTEX [30].

The X-ray photoelectron spectra were acquired using a monochromated Al *K*α X-ray source (1486 eV, 10 mA emission at 150 W) for surface sensitive X-ray photoelectron spectroscopy (XPS) measurements. Charge neutralisation for insulating samples was achieved using a low energy electron flood source as required (FS40A, PreVac). Binding energy scale calibration was performed either using C-C in the C 1*s* photoelectron peak at 285 eV or using Au $4f_{7/2}$ at 84 eV, else the Fermi level at 0 eV, of a clean gold reference sample. Analysis and curve fitting were performed using Shirley backgrounds with GL(50) Voigt-approximation peaks using CasaXPS [31].

Fourier transform infrared (FTIR) spectra were acquired using a Shimadzu IRAffinity 1S IR Spectrometer.

The photocurrent *versus* voltage (J-V) characteristics of the devices were evaluated under simulated AM 1.5G radiation (illumination intensity of 100 mW cm^{-2}) by using a Sciencetech solar simulator (SS150-AAA) and a source meter (Keithley 2401). The solar cells were applied with a bias voltage sweep ranging from -0.20 V to 1.5 V, with a voltage step of 0.05 V and a delay time of 0.200 seconds. The light intensity was calibrated using a standard silicon solar cell (ORIEL® PV Reference Cell System; Model number 91150V, certified by NREL) before undertaking J-V measurements.

The external quantum efficiency (EQE) of the PSCs were measured at zero bias by illuminating the devices with a monochromatic light source using a Xenon lamp in combination with a dual-grating monochromator from Bentham Instruments. The number of photons incident on the samples were calculated for each wavelength using a silicon photodiode calibrated by the National Physical Laboratory.

For the indoor measurements, four different light sources were used, namely, PRO-ELEC daylight white light-emitting diode (LED) (11 W, 6500K, intensity 0.25 mW cm^{-2}), OSRAM cool white LED (8.5 W, 4000 K, intensity 0.25 mW cm^{-2}), OSRAM warm white LED (806 lm Classic A 60, 8.5 W, 2700 K, intensity 0.30 mW cm^{-2}), and a cool white compact fluorescent lamp (CFL) (23 W, 4000 K, intensity 0.25 mW cm^{-2}). The luminous intensity was measured using a lux meter and all indoor lamps were set at 1000 lux illuminance.

3. Results and Discussion

(a) Photovoltaic properties

Figure 1 (a) shows the schematic of the n-i-p device architecture [Glass/ITO/SnO_2/$CsPbIBr_2$/Spiro-OMeTAD/Au] used in this study for the fabrication of the of the $CsPbIBr_2$ devices. Depending on their location inside buildings, various types of illumination are used indoors and hence, the photovoltaic properties of the optimised $CsPbIBr_2$ devices were characterised under different indoor lamps, namely, daylight white LED, warm white LED, cool white LED, and CFL. The emission spectra of the indoor illumination sources used in this study are shown in **Figure 1 (b)**. The maximum PCE demonstrated by the optimised devices were 9.4%, 8.7% and 6.3% under cool white LED, CFL and warm white LED, respectively. The photovoltaic parameters are summarised in Table S1 (Supplementary Information). The performance was found to be best in the case of daylight white LED due to the maximum spectral match between daylight white LED and the EQE spectra. The current density *versus* voltage (J-V) characteristics of the champion devices with the photovoltaic

performance parameters measured under daylight white LED in forward and reverse scans are shown in **Figure 1 (c)**. These devices recorded champion photovoltaic parameters with a PCE of 14.1%, short circuit current (J_{SC}), open circuit voltage (V_{OC}) and fill factor (FF) as 0.06 mA cm^{-2}, 0.95 V and 61.6%, respectively, in reverse scan. The current density and PCE under a steady state voltage bias of 0.7 V are shown in **Figure 1 (d)**. A steady state PCE of 8.8% was obtained under constant indoor light illumination of 1000 lux. **Figure 1 (e)** shows the corresponding J-V characteristics of the best device under 1 Sun condition. The PCE values were recorded as 5.3% and 5.9% in forward and reverse scans, respectively, with a very low hysteresis index of ~10%. The corresponding photovoltaic parameters were recorded as 8.51 mA cm^{-2}, 1.01 V and 68.4% for the J_{SC}, V_{OC} and FF, respectively, in reverse scan. The stabilized current density and PCE were measured as ~4.3 mA cm^{-2} and ~3.5%, respectively, under 0.8 V bias under 1 Sun continuous illumination **[Figure 1 (f)]**. The longer stabilisation time for the J_{SC}/PCE under indoor light as compared to 1 Sun can be attributed to the higher hysteresis effect of these devices under low-intensity illumination as is evident from a comparison between Figure 1 (c) and Figure 1 (e). The higher J-V hysteresis effect in halide perovskite photodiodes under low-intensity illumination has been recently reported by Zhou *et al*. [32].

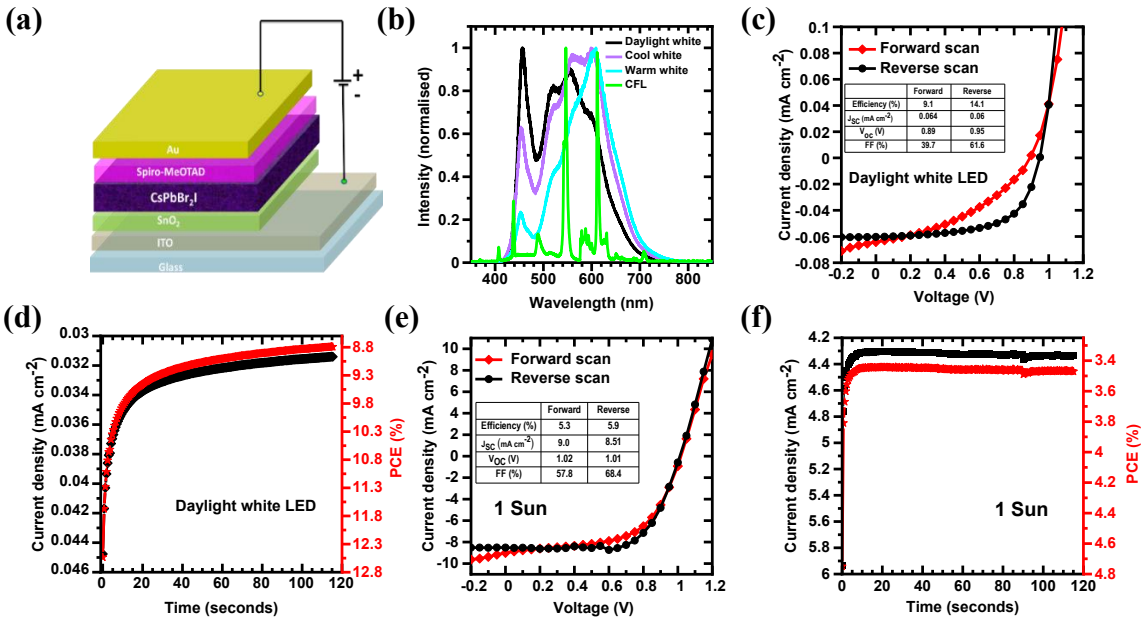

Figure 1 (a) Device architecture of the n-i-p devices used in this study. (b) Spectra of the different indoor lamps used in this study. (c & e) Current density *versus* voltage curves for the best performing device in forward and reverse scans along with the photovoltaic parameters

under (c) daylight white LED light and (e) 1 Sun illumination. (d & f) Steady state tracking of the current density and PCE under (d) daylight white LED (voltage bias ~ 0.7 V) and (f) 1 Sun condition (voltage bias ~ 0.8 V).

The performance reproducibility of the optimised $CsPbIBr_2$ devices under daylight white LED and 1 Sun is shown in **Figures 2 (a) and (b)**. *The fabrication of devices was repeated four times with each set of measurements being undertaken on at least 24 photovoltaic devices and the photovoltaic parameters were averaged over the working devices.* Not only was the device performance reproducible but also the devices showed appreciable stability under ambient conditions as will be discussed in detail in the later sections. The external quantum efficiency (EQE) spectrum in **Figure 2 (c)** shows that the light harvesting ability of the $CsPbIBr_2$ photovoltaic devices approaches 60% in the bulk of the visible spectrum. The integrated J_{SC} calculated from the EQE spectrum was 7.2 mA cm^{-2} which is quite consistent with the J_{SC} from the J-V measurements under 1 Sun. These $CsPbIBr_2$ films with these excellent photovoltaic properties were obtained after a series of optimisation steps as discussed in the next section.

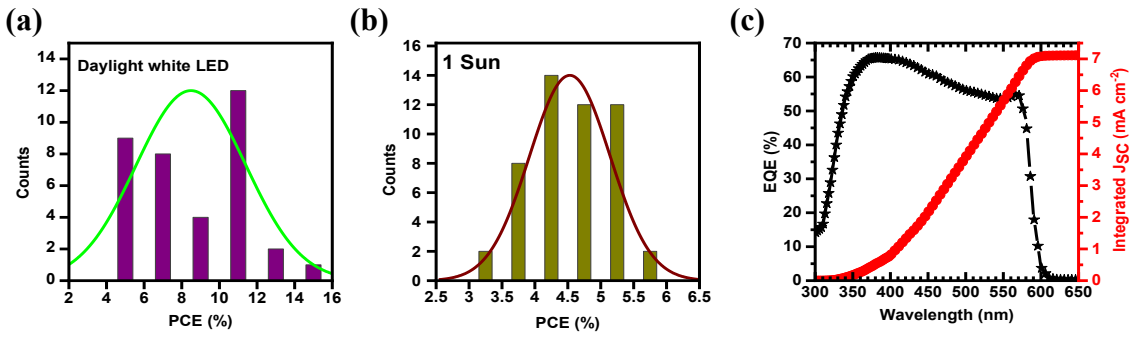

Figure 2 (a & b) PCE distribution of 36 and 50 devices under daylight white LED (1000 lux) and 1 Sun illumination conditions, respectively. (c) External quantum efficiency spectrum with the integrated short circuit current for the $CsPbIBr_2$ perovskite devices.

(b) Optimisation of $CsPbIBr_2$ films and photovoltaic devices

$CsPbIBr_2$ films were fabricated without and with anti-solvent treatment and systematically characterised using scanning electron microscopy (SEM), UV-Vis spectroscopy, X-ray diffraction (XRD), electron backscattered diffraction (EBSD) and X-ray photoelectron spectroscopy (XPS). The selected anti-solvents were diethyl ether and chlorobenzene. The UV-visible absorption spectra of freshly prepared $CsPbIBr_2$ perovskite

films (thickness ~240 nm), irrespective of the anti-solvent treatment, show the same position of the absorption peak [**Figure 3 (a)].** The absorption onset is observed at ~600 nm corresponding to a bandgap of ~2.09 eV and is in good agreement with previous reports [19,33–35] [Inset of Figure 3 (a) shows the Tauc plot]. The crystallinity of the pristine, chlorobenzene and diethyl ether treated $CsPbIBr_2$ perovskite films was investigated using XRD measurements. As can be seen from **Figure 3 (b)**, characteristic peaks at 15.24°, 21.52°, 30.42°, 34.14° and 37.37° corresponding to the (100), (110), (200), (210) and (211) planes of the cubic α-phase $CsPbIBr_2$ perovskite structure are observed in all three cases [10,16,36]. The intensity of the (100) and (200) crystal planes is lowest in the case of chlorobenzene treated $CsPbIBr_2$ films, which suggests their inferior crystalline quality compared to the pristine and diethyl ether anti-solvent treated films [Figure S1]. However, a closer look at the peaks shows the slight displacement of the (100) and (200) peak positions due to the usage of different anti-solvents [Figure S1]. Diethyl ether treatment has resulted in shifting the peak positions to lower angles, thus, suggesting an expansion of the crystal lattice. This implies the better incorporation of iodide ions into the $CsPbIBr_2$ crystal lattice.

The secondary electron (SE) images of the $CsPbIBr_2$ films obtained using scanning electron microscopy are shown in **Figure 3 (c)**. In the case of perovskite films fabricated without any anti-solvent treatment, discrete cube-like features are observed which appears to lack both continuity and surface coverage [**Figure 3 (c) (i)**]. The surface morphology becomes dense and compact and surface coverage improves upon anti-solvent treatment as can be seen from **Figures 3 (c) (ii) and (iii).** The chlorobenzene treated $CsPbIBr_2$ films show the presence of randomly sized grain-like features ranging from 100 nm to 500 nm and the presence of pinholes [**Figure 3 (c) (ii)**]. A compact perovskite film with no pinholes and with grain-like domains ~500 nm in size is formed after diethyl ether treatment [**Figure 3 (c) (iii)**]. The term grain is used with caution here, as there is wide debate regarding grain and grain boundaries in the hybrid perovskites [37,38]. With these results from the optimisation of $CsPbIBr_2$ films, n-i-p photovoltaic devices were fabricated using chlorobenzene and diethyl ether as anti-solvents and characterised under both indoor artificial lights and outdoor 1 Sun spectra. Tables S2 and S3 summarize the corresponding photovoltaic performance parameters and the detailed description of the photovoltaic device optimization is given in the Supplementary Information.

Distribution of the photovoltaic parameters under 1 Sun for the devices fabricated without anti-solvent and with chlorobenzene and diethyl ether treatment are shown in **Figure 3 (d)**. Despite the incomplete surface coverage [Figure 3 (c) (i)], devices without anti-solvent

treatment demonstrated a wide range of PCE values from ~2 - 5.9%. This suggests the presence of a thin layer of $CsPbIBr_2$ film on the surface which connects the discrete cube-like domains observed in the secondary electron images. Devices with diethyl ether treatment demonstrated higher PCE values with lower distribution range and best efficiency of 5.9%. Hence, the average hysteresis index was also lower in case of the diethyl ether treated devices (~17%) compared to those without any anti-solvent treatment (~21%). The V_{OC} distribution was quite wide, ranging from ~0.75 V - 1.1 V in case of devices without anti-solvent, whereas majority of the diethyl ether treated devices showed V_{OC} between 0.9 V and 1.1 V. The J_{SC} values were quite widespread, irrespective of sample preparation, however, the diethyl ether treated devices recorded higher J_{SC} on an average. The distribution of FF during forward scan was comparable in either case, ranging from ~40 - 58%, whereas the diethyl ether treated devices recorded considerably higher reverse scan FF (>60 - 80%) compared to devices without anti-solvent treatment (~55 - 70%). The comparatively better device performance with lesser variation in PCE values for devices fabricated with diethyl ether can be attributed to the improved perovskite crystallinity, grain size and surface coverage upon diethyl ether treatment [Figure 3 (c) (iii)]. This implies that diethyl ether anti-solvent treatment facilitates nucleation by rapidly reducing the precursors solubility which results in better crystallization and formation of large perovskite grains. *Devices fabricated using chlorobenzene treated $CsPbIBr_2$ films recorded the lowest photovoltaic parameters despite their improved surface coverage and dense, compact surface morphology. This poor device performance can be attributed to the presence of pinholes and inferior crystalline quality of these films as revealed through the corresponding SEM image [Figure 3 (c) (ii)] and XRD pattern [Figure 3 (b) and Figure S1]. The pinholes in the photoactive perovskite layer can induce shunting paths and promote undesirable charge recombination, resulting in poor device performance.*

Figures 3 (e) compares the J-V characteristics of the best performing $CsPbIBr_2$ perovskite-based devices without anti-solvent, and with chlorobenzene and diethyl ether treatment under 1 Sun illumination. Devices without anti-solvent treatment showed a champion PCE of 5.9% in the reverse scan with J_{SC}, V_{OC} and FF being 7.9 mA cm^{-2}, 1.14 V and 65.1%, respectively. The J_{SC} and FF improved with diethyl ether treatment, recording 8.5 mA cm^{-2} and 68.1%, respectively. The inferior performance of devices without anti-solvent treatment, coupled with their rapid degradation to the non-perovskite phase during 1 Sun measurement may be attributed to the formation of nucleation sites for phase segregation. Diffusion of Li^+ ions from Spiro-OMeTAD upon air exposure or the interaction of mobile iodide species of the

perovskite with Spiro-OMeTAD at the perovskite/hole-selective interface may facilitate growth of the non-perovskite phase due to the improper surface coverage which detrimentally affects the device stability [39–42].

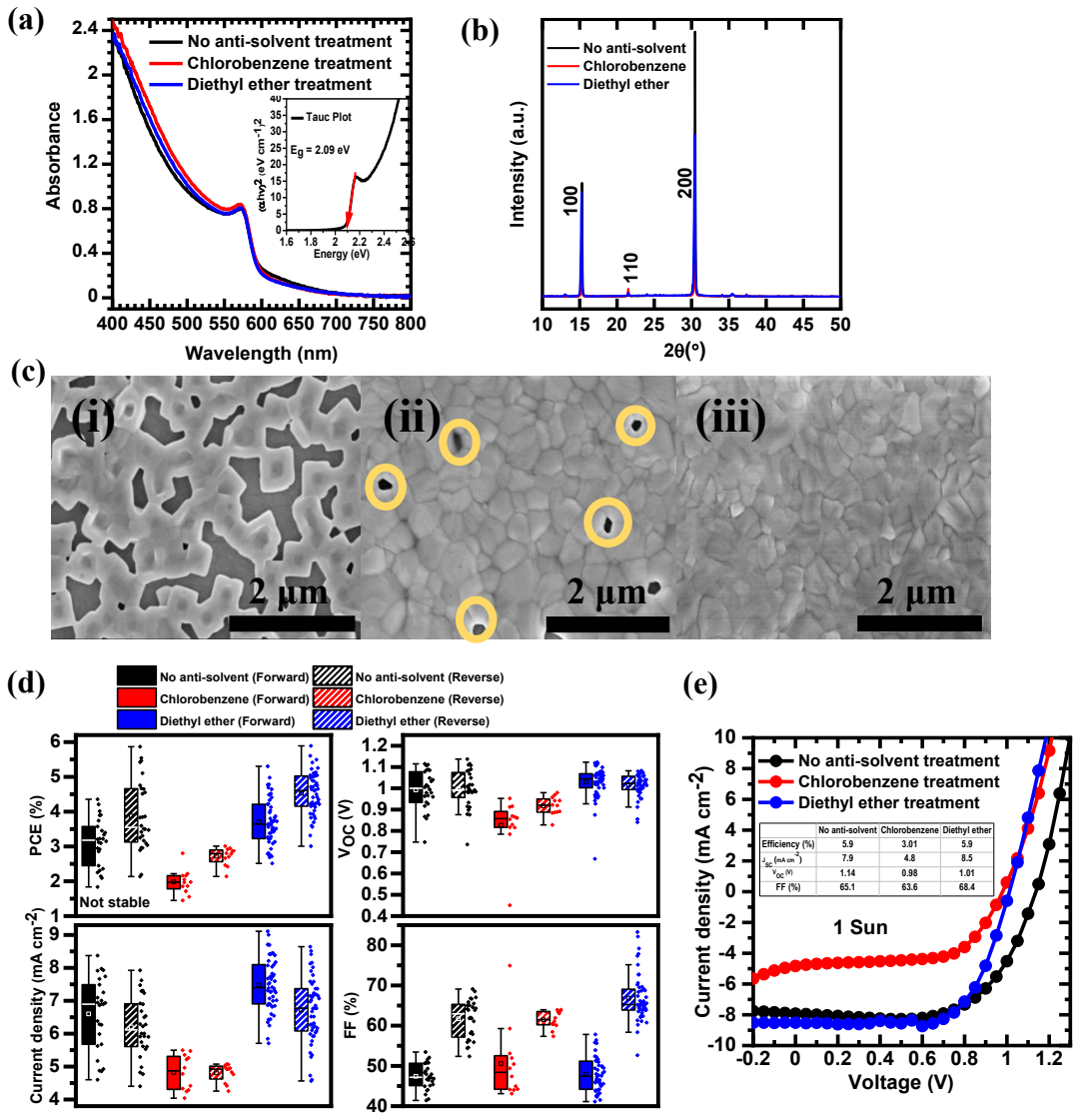

	No anti-solvent	Chlorobenzene	Diethyl ether
Efficiency (%)	5.9	3.01	5.9
J_{SC} (mA cm^{-2})	7.9	4.8	8.5
V_{OC} (V)	1.14	0.98	1.01
FF (%)	65.1	63.6	68.4

Figure 3 (a) Absorption spectra of pristine $CsPbIBr_2$ films with no anti-solvent wash, chlorobenzene, and diethyl ether treatment (Inset is the Tauc plot showing the band gap of the $CsPbIBr_2$ perovskite film as 2.09 eV). (b) X-ray diffractograms of $CsPbIBr_2$ films fabricated without anti-solvent wash, chlorobenzene, and diethyl ether treatment. (c) Morphology studied using scanning electron microscopy of $CsPbIBr_2$ films with (i) no anti-solvent treatment, (ii) chlorobenzene (presence of pinholes shown as yellow circles), and (iii) diethyl ether treatment.

(d) (Clockwise from top left) Distribution of photovoltaic parameters PCE (%), V_{OC} (V), FF (%) and J_{SC} (mA cm^{-2}) for devices fabricated without anti-solvent treatment, with chlorobenzene, and diethyl ether in forward and reverse scans under 1 Sun. (e) Current density *vs* voltage curves for the best performing devices with no anti-solvent treatment, chlorobenzene, and diethyl ether treatment along with the respective photovoltaic parameters under 1 Sun in reverse scan.

For the corresponding indoor illumination performance, devices fabricated using diethyl ether treated perovskite films showed the best efficiency under daylight white LED, recording 9.1% and 14.1% under forward and reverse scans, respectively. Though the photovoltaic parameters of these devices were comparable to those fabricated without any anti-solvent treatment (9.9% and 13.6% during forward and reverse scans, respectively), the latter devices rapidly degraded to yellow, non-perovskite phase during the measurements [Figure S2 and Table S3]. Devices fabricated using chlorobenzene treated $CsPbIBr_2$ films were not studied under low-intensity indoor illumination since they recorded the lowest photovoltaic parameters under 1 Sun and degraded rapidly during measurement. Devices with diethyl ether treatment not only demonstrated the best device performance under both 1 Sun and indoor illumination but also enhanced air-stability compared to the other devices. Hence, the volume optimisation for anti-solvent treatment was undertaken with diethyl ether and devices fabricated with the optimised volume of 750 µL demonstrated the champion PCE of 5.9% with low hysteresis, good repeatability of device performance, and improved air-stability. Details of the optimisation process is discussed in the Supplementary Information (Figures S3 & S4 and Table S4).

To understand the difference in photovoltaic device performance, as well as ambient stability of the diethyl ether anti-solvent treated $CsPbIBr_2$ films, detailed microstructural and spectroscopic characterisation using EBSD, XPS and Fourier transform infrared (FTIR) spectroscopy were carried out on both pristine and anti-solvent treated $CsPbIBr_2$ films and partial device heterostructures. Since the secondary electron images cannot provide any crystallographic information, EBSD measurements were performed to accurately identify crystalline grain properties (size, homogeneity and misorientation) [43].

(c) Microstructural and compositional analysis

Figures 4 (a)-(c) show the SE images of the areas probed using EBSD, where the three samples ($CsPbIBr_2$ films) without anti-solvent, with chlorobenzene and diethyl ether treatment, respectively, were tilted by 70˚. The EBSD band contrast images in **Figures 4 (d)-(f)** already

indicate the grains present in the films, with grain boundaries giving lower contrast. Inverse pole figure (IPF) Z maps, as displayed in **Figures 4 (g)-(i)**, of the $CsPbIBr_2$ perovskite crystals for the three films provide the crystallographic directions in the Z direction, which is the sample normal. The sample without anti-solvent treatment showed a strong preference for the (100) plane (or [100] direction) for crystalline grain orientation [Figure 4 (g)], whereas the (100) orientation is less dominant, with other orientations also observed in case of the films with chlorobenzene and diethyl ether treatment [Figures 4 (h) and (i), respectively]. To investigate this orientation relationship further, **Figures 4 (j)-(l)** show the pole figures of the (100) plane for the three $CsPbIBr_2$ films (note the same scale applies to all three pole figures). For the film without anti-solvent treatment, the majority of data points are at the centre of the hemisphere, confirming that most grains are (100) oriented [Figure 4 (j)]. For the samples treated with anti-solvents (chlorobenzene and diethyl ether), the spot at the centre is less dominant and additional spots appear in the respective pole figures [Figures 4 (k) and (l), respectively], compared to the films without anti-solvent treatment. **Figure S5** shows the IPF maps for the sample X, Y and Z directions for the three $CsPbIBr_2$ films, without and with anti-solvent treatment. **Figure S6** shows the same pole figures on individual scales, showing that (100) is still the dominant orientation for all samples. This agrees well with the XRD results in Figure 3 (b).

Previously Jariwala *et al*. have reported that orientational heterogeneities within the grains enhance the non-radiative recombination [38]. To unravel any crystalline orientational heterogeneity, the grain misorientation was calculated in terms of grain orientation spread (GOS) and grain reference orientation deviation (GROD) angle for all the $CsPbIBr_2$ films without and with anti-solvent treatment as seen in **Figures 4 (m)-(o)** and **Figures 4 (p)-(r)**, respectively. The GOS is the mean misorientation of a given grain, whereas the GROD angle provides the deviation of each pixel within a grain from the mean misorientation (GOS) of that grain. The mean GOS, calculated from all grains, decreases upon treatment with diethyl ether (0.39 ± 0.03^{o}) and chlorobenzene (0.47 ± 0.06^{o}) compared to films without any anti-solvent treatment (0.68 ± 0.18^{o}). This can be seen in **Figure 4 (m)** for the sample without any treatment, where more grains with a larger GOS can be observed compared to the samples treated with anti-solvents which exhibit a more uniform GOS with fewer grains of larger misorientation [**Figure 4 (n)-(o)]**. The GROD angle maps in **Figures 4 (p)-(r)** show an analogous behaviour. The grains with larger mean misorientations (i.e., larger GOS) also exhibit larger GROD angle values. This implies that grains with a large GOS also possess large misorientation within their boundaries. This is most dominant for the $CsPbIBr_2$ film without anti-solvent treatment. The

film with diethyl ether treatment exhibits the least amount of misorientation between grains and within a given grain compared to the other two samples. This implies that the $CsPbIBr_2$ films without anti-solvent and with chlorobenzene treatment have the highest degrees of crystalline orientational heterogeneity, and/or most likely, variation in local strain and hence, will suffer from more non-radiative recombination [38,43–45]. *Previous studies have shown that local strain can accelerate the device degradation by reducing the ion migration activation energy [46]. Thus, the misorientation induced local strain can also contribute to the faster degradation observed for the devices having $CsPbIBr_2$ films without any antisolvent and with chlorobenzene treatment.* The complete surface coverage and lowest misorientation heterogeneity of the diethyl ether treated $CsPbIBr_2$ films can thus account for the best photovoltaic device performance.

According to the previous reports, an inhomogeneous distribution of grain size can be a limiting factor of microscopic properties in halide perovskite films [43]. For the small number of grains imaged by EBSD for these three samples, no significant difference in grain size was observed. All three samples exhibit comparable mean grain sizes and grain size variability. The mean area, mean perimeter and mean circle equivalent diameter are shown in **Table S5**. The significant difference between the samples revealed by EBSD is the misorientation within the grains.

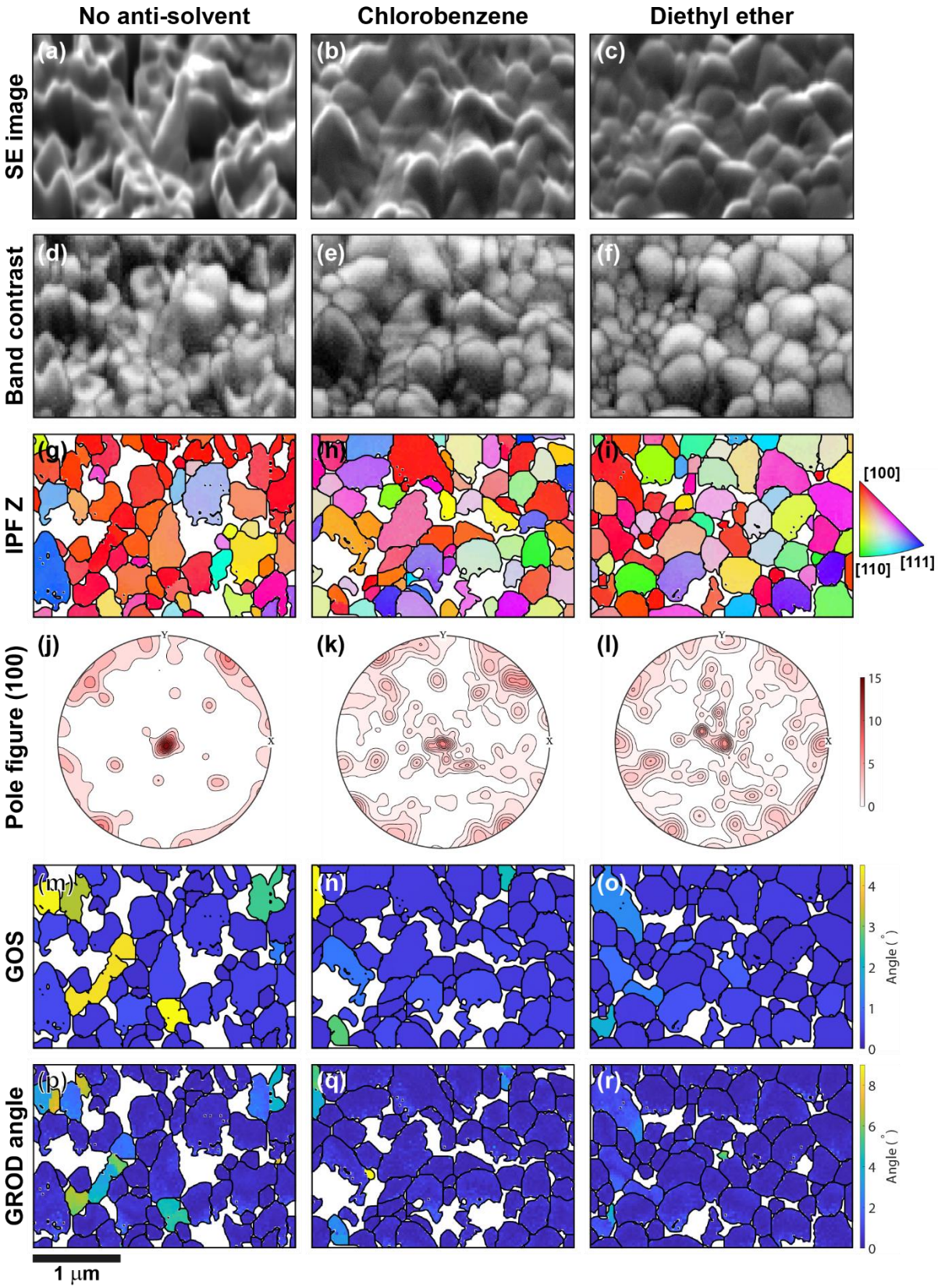

Figure 4 SE images (a)-(c), band contrast images (d)-(f), IPF Z maps (the colour key on the right applies to all three IPF maps) (g)-(i), (100) pole figures (j)-(l), GOS maps (m)-(o) and GROD angle maps (p)-(r) derived from EBSD measurements of the $CsPbIBr_2$ films without

anti-solvent treatment (first column), with chlorobenzene (second column) and diethyl ether (third column) treatment, respectively.

The surface elemental composition and chemical states of the $CsPbIBr_2$ perovskite films on ITO, prepared without and with anti-solvent treatment, were probed using XPS to correlate the compositional features with their device performance. Clear signature peaks of Cs, Pb, I, and Br, from the $CsPbIBr_2$ films are detected with a negligible amount of carbon and without any other impurity peak which can be regarded as indicators of compositional purity of the samples **(Figure S7)** (Adventitious carbon is commonly expected in any *ex-situ* prepared sample). The high-resolution Cs 3*d*, Pb 4*f*, I 3*d* and Br 3*d* core level spectra are shown in **Figure 5**. The Cs 3*d* doublet is observed at 724.5±0.1 eV and 738.5±0.1 eV corresponding to Cs $3d_{5/2}$ and Cs $3d_{3/2}$ with a spin-orbit splitting of 13.9 eV [Figure 5 (a)] whereas the peaks at 138.4±0.1 eV and 143.1±0.1 eV are attributed to Pb $4f_{7/2}$ and Pb $4f_{5/2}$, respectively [Figure 5 (d)]. The spectra of the two halides, i.e. iodide (I 3*d*) and bromide (Br 3*d*) are observed at 619.0±0.2 eV and 630.4±0.1 eV, assigned to I $3d_{5/2}$ and I $3d_{3/2}$ (splitting of 11.5 eV) [Figure 5 (b)], and at ~68.5 - 70.0 eV, respectively [Figure 5 (c)]. The peak positions and spin-orbit splitting in all the samples are very similar to the previously reported literature [9,23]. There is no appreciable variation in the Cs 3*d* and I 3*d* core levels because of treatment with different anti-solvents **[Figure 5 (a) and (b)].** The Br 3*d* spectra have been fitted with two components corresponding to Br $3d_{5/2}$ and Br $3d_{3/2}$ at ~68.1 and 69.3 eV, respectively, and does not show any variation due to the different anti-solvent treatment techniques followed in this study [**Figure 5 c (i – iii)**].

The Pb 4*f* spectra for all films irrespective of preparation technique, consist of two separate contributions from $4f_{7/2}$ and $4f_{5/2}$ peaks with a ratio of ~1.25 and spin-orbit splitting of 4.8 eV. The primary Pb $4f_{7/2}$ peak is found at 138.4±0.1 eV, consistent with the Pb $4f_{7/2}$ binding energy attributed to Pb (II) in the perovskite structure [47,48]. Two smaller, yet evident peaks are detected at ~136.9±0.2 and 141.8±0.2 eV corresponding to Pb $4f_{7/2}$ and Pb $4f_{5/2}$, respectively, in all samples, which can be attributed to the presence of metallic Pb (Pb^0) [**Figures 5 (d) and (e)**]. This component has previously been reported as defect sites and regarded as recombination centres for the charge carriers in the perovskite film which are detrimental to device performance [48]. Though the presence of metallic Pb is observed irrespective of the sample preparation, the fraction of the Pb^0 signal shows significant variation depending on the anti-solvent treatment [Figure 5 (e)]. The quantification was performed after careful peak fitting of each component of the Pb 4*f* doublet using CasaXPS with the residue $\chi^2<0.5$. *Figure*

5 (e) shows the variation in the fraction of the Pb^0 signal of the Pb4f core level as a function of different the anti-solvent treatment processes with sub-part (i) showing the spectrum without anti-solvent treatment, (ii) after chlorobenzene and (iii) for diethyl ether treatment, respectively. From the figure 5 (e) it is observed that the area under the curve reduces from (i) to (ii) to (iii) which implies a monotonic decrease in both Pb^0 components (Pb^0 $4f_{7/2}$ and Pb^0 $4f_{5/2}$) due to anti-solvent treatment. Samples without anti-solvent treatment demonstrate a Pb^0/Pb^{2+} fraction of ~0.034 [atomic% of Pb^0 ~ 2.07% (Pb $4f_{7/2}$) and 1.20% (Pb $4f_{5/2}$)] which reduces to ~0.025 upon chlorobenzene treatment [atomic% 1.35% (Pb $4f_{7/2}$) and 1.08% (Pb $4f_{5/2}$)] and further to ~0.010 after diethyl ether treatment, implying a much lesser metallic Pb defect concentration. This low metallic Pb content in diethyl ether treated $CsPbIBr_2$ films can explain the better photovoltaic performance of the corresponding devices [**Table S2, Figures 3 (d) and (e)**]. The evolution of metallic Pb has been previously correlated with the loss of iodine from the perovskite lattice [49]. Thus, the low content of metallic Pb in the diethyl ether treated $CsPbIBr_2$ films in turn suggests better incorporation of Pb and iodine into the lattice and correlates well with the finding from the XRD analysis (better incorporation of iodide ions into the $CsPbIBr_2$ crystal lattice).

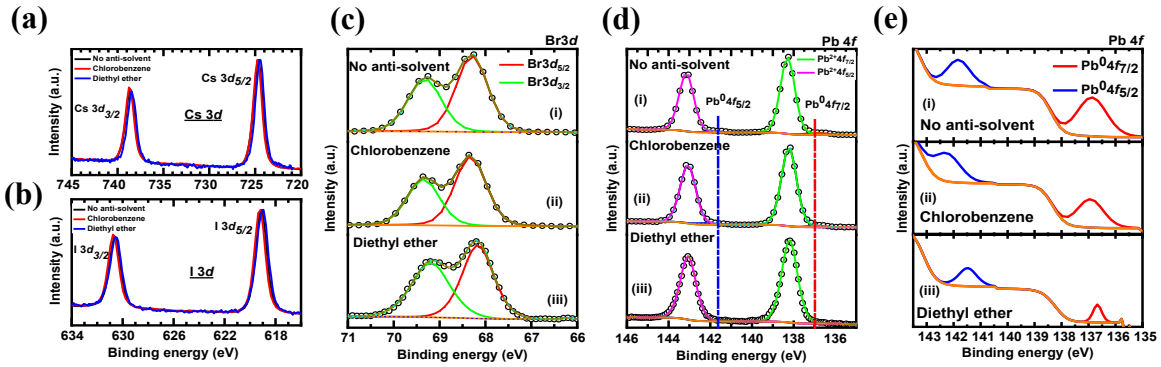

Figure 5 High resolution XPS core level spectra (a) Cs 3*d*, (b) I 3*d,* (c) Br 3*d,* and (d) Pb 4*f* of $CsPbIBr_2$ films prepared (i) without anti-solvent treatment (ii) with chlorobenzene and (iii) diethyl ether treatment, respectively. (e) Section of the Pb 4*f* spectra showing the metallic lead (Pb^0 4*f*) components only.

Though the microstructural and compositional analysis of the $CsPbIBr_2$ films prepared without and with anti-solvent treatment revealed the reason for the enhanced photovoltaic performance of devices with the diethyl ether treated $CsPbIBr_2$ films, the understanding of enhanced stability was still lacking. Hence, time-dependent stability characterisation of $CsPbIBr_2$ photovoltaic devices and partial heterostructures was carried out.

(d) Stability of $CsPbIBr_2$ photovoltaic devices

During 1 Sun measurements, the devices without any anti-solvent and with chlorobenzene treated $CsPbIBr_2$ films were observed to be undergoing degradation from the brown perovskite phase to the yellow non-perovskite phase. The X-ray diffraction patterns of the phase-changed $CsPbIBr_2$ film and Glass/ITO/SnO_2/$CsPbIBr_2$/Spiro-OMeTAD/Au device stack due to ageing in air are shown in **Figure S8**. The peak at 10.24° can be assigned to the δ-phase of $CsPbIBr_2$ [10,36,50–52]. This peak is visible in both the $CsPbIBr_2$ film and the $CsPbIBr_2$ based device stack, clearly demonstrating that the freshly deposited α-phase of the $CsPbIBr_2$ perovskite has degraded into the yellow non-perovskite orthorhombic δ-phase after ageing in air. Photographs of the degraded solar cell device stack without and with different anti-solvents as observed from the Glass/ITO side are shown in Figure S9 (A/B - no anti-solvent treatment, C/D - chlorobenzene treatment, and E/F - diethyl ether treatment).

The stability of the Glass/ITO/SnO_2/$CsPbIBr_2$/Spiro-OMeTAD partial heterostructure was studied using FTIR spectroscopy to understand the role of the perovskite/Spiro-OMeTAD interface in the degradation of devices since the pristine $CsPbIBr_2$ films were very stable in ambient conditions. The degradation behaviour of the partial heterostructures was found to follow the same pattern as that of the completed photovoltaic devices with Au top electrode; that is, the $CsPbIBr_2$ perovskite phase transformed into the non-perovskite phase in less than 2 hours for the films without anti-solvent treatment whereas diethyl ether treated films were stable for longer (more than 8 hours) under humidity of 33%, with the chlorobenzene treated films in the intermediate range of hours. Previous studies have shown that the degradation observed in hybrid perovskite devices under high humidity can be assigned to the hygroscopic nature of the Li-TFSI dopant used for improving the hole mobility and conductivity of Spiro-OMeTAD hole conductor which in turn facilitates moisture ingress into the perovskite layer, thus, resulting in progressive deterioration of devices [53–55]. Detailed FTIR characterization (Supplementary Information and **Figure S10**) revealed that Spiro-OMeTAD conjugation disruption is faster in films without any anti-solvent. The rapid device degradation in devices without anti-solvent treatment can be attributed to the aggregation of hygroscopic Li^+ in the regions with thinner $CsPbIBr_2$ films due to the lower surface coverage than films with diethyl ether treatment. These localized regions of high moisture content would also be more susceptible to the formation of nucleation sites for the non-perovskite yellow phase due to interaction between mobile iodide species with the Spiro-OMeTAD at the hole-selective

interface [42]. Thus, the perovskite surface coverage and Spiro-OMeTAD/perovskite interface plays an important role in the ambient stability of $CsPbIBr_2$/Spiro-OMeTAD devices.

Even though the previous reports have demonstrated $CsPbIBr_2$ devices with better PCE values, the stability test for those devices were carried out only either under inert ambient or inside the glovebox [22,35,56]. *However, in the present study,* the shelf-life stability of the unencapsulated completed device structure fabricated using diethyl ether treated $CsPbIBr_2$ was investigated under near ambient conditions. The variation in normalized PCE of these devices is shown in **Figure 6** with the inset showing the images of the devices (from both Au and Glass sides) after storage in a desiccator (humidity ~30%) for 40 days. *The shelf-life stability of the unencapsulated devices was investigated in ambient air under RH of 33%, every couple of days for about two months. Between measurements, the devices were stored in the dark at RH of ~30%. The devices retained >68% of their maximum PCE after 27 days despite being unencapsulated and this PCE reduced to >55% after 40 days of storage, decreasing eventually to 51% after two months.* This kind of stability value is one of the best reported so far for $CsPbIBr_2$ films. *In addition to the enhanced shelf-life stability, the present study demonstrates the promising potential of $CsPbIBr_2$ devices fabricated at a processing temperature low enough to be compatible with flexible PET substrates to maximise the chances of integration while implementing the devices as indoor light harvesters to autonomously power the sensors for the IoT. Moreover, the present study will provide a fresh perspective for research on Cs-based indoor photovoltaic devices and along with the already published reports, help strengthen the understanding of the role of surface morphology and composition of Cs-based perovskite semiconductors on device performance especially under indoor illumination.* Preliminary attempts were made to use these $CsPbIBr_2$ devices for powering a non-inverting buffer with open-drain output under indoor light (0.25 mW cm^{-2}) as discussed in the Supplementary Information **(Figure S11)**.

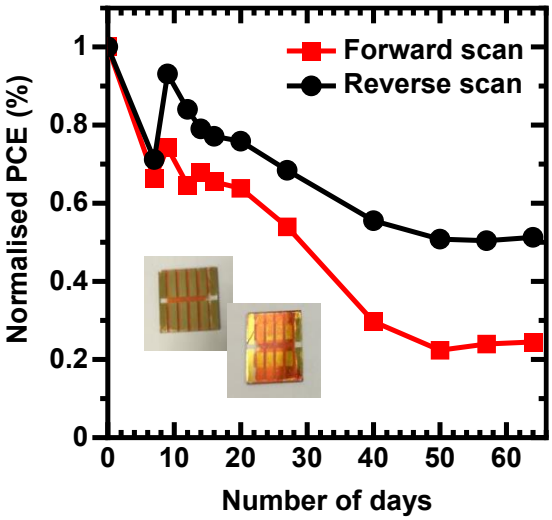

Figure 6 Variation in normalized power conversion efficiency of the optimized $CsPbIBr_2$ perovskite solar cells studied as a function of the number of days; inset shows the photographs of the diethyl treated $CsPbIBr_2$ based devices after 40 days storage in RH 30%.

4. Conclusions

In summary, highly crystalline and compact $CsPbIBr_2$ perovskite based photovoltaic devices were fabricated in n-i-p configuration with a PCE of 14.1% under indoor illumination at 1000 lux illuminance. Detailed investigation of the surface morphology demonstrated that the selection of anti-solvent was of critical importance in obtaining the desired dense and compact $CsPbIBr_2$ perovskite morphology with excellent surface coverage and improved air-stability of the devices. In-depth microstructural characterisation undertaken in this study revealed that diethyl ether anti-solvent treatment was effective in reducing the defect concentration in the form of metallic Pb, and in suppressing the grain misorientation in $CsPbIBr_2$ films which resulted in improved performance of the corresponding photovoltaic devices. The optimised devices also retained >55% of the maximum PCE after storage in 30% relative humidity for more than 40 days. The ambient stability of $CsPbIBr_2$/Spiro-OMeTAD devices was influenced by the perovskite surface coverage as well as the Spiro-OMeTAD/perovskite interface. The low temperature annealed, efficient and stable all-inorganic $CsPbIBr_2$ perovskites developed in this study not only shows promise of compatibility with flexible and wearable substrates but also for powering next-generation electronic devices in the IoT.

Data Accessibility

The research data underpinning this publication can be accessed at https://doi.org/10.17630/970ac996-d043-48f8-bf70-7c0eb33f7b9a [REF].

CRediT authorship contribution statement

Paheli Ghosh: Methodology, Investigation, Data Acquisition, Formal analysis, Data curation, Writing - original draft, Writing - review & editing. Jochen Bruckbauer: Acquisition, Investigation, and Analysis of EBSD data, Writing - original draft (section on EBSD), Writing - review & editing. Carol Trager-Cowan: Acquisition, Investigation, and Analysis of EBSD data, Writing - review & editing. Lethy Krishnan Jagadamma: Conceptualization, Methodology, Data Acquisition, Formal analysis, Writing - original draft, Writing - review & editing, Supervision, Funding acquisition, Project administration.

Declaration of competing interest

The authors declare that they have no known competing financial or other interests that could have appeared to influence the work reported in this paper.

Acknowledgement

LKJ acknowledges funding from UKRI-FLF through MR/T022094/1. LKJ acknowledges Professor Ifor D. W. Samuel and Professor Graham A. Turnbull for the kind permission to access 1 Sun and EQE measurements. LKJ and PG acknowledge Dr Ben F. Spencer for the XPS data acquisition, which was supported by the Henry Royce Institute, funded through UK EPSRC grants EP/R00661X/1, EP/P025021/1 and EP/P025498/1 and Dr Julia L. Payne for the arrangements with XRD and FTIR measurements. JB and CTC acknowledge funding from UK EPSRC grant EP/P015719/1.

References

[1] K. Ruhle, M. Kasemann, Approaching high efficiency wide range silicon solar cells, Conf. Rec. IEEE Photovolt. Spec. Conf. (2013) 2651–2654.

[2] I. Raifuku, Y. Ishikawa, S. Ito, Y. Uraoka, Characteristics of Perovskite Solar Cells under Low-Illuminance Conditions, J. Phys. Chem. C. 120 (2016) 18986–18990.

[3] H.K.H. Lee, J. Barbé, W.C. Tsoi, Organic and perovskite photovoltaics for indoor applications, Elsevier Ltd, 2019.

[4] M.F. Müller, M. Freunek, L.M. Reindl, Maximum efficiencies of indoor photovoltaic devices, IEEE J. Photovoltaics. 3 (2013) 59–64.

[5] J.K.W. Ho, H. Yin, S.K. So, From 33% to 57%-An elevated potential of efficiency limit for indoor photovoltaics, J. Mater. Chem. A. 8 (2020) 1717–1723.

[6] NREL, Best Research Cell Efficiencies, (2021).

[7] J. Zhang, G. Hodes, Z. Jin, S. Liu, All-Inorganic CsPbX3 Perovskite Solar Cells: Progress and Prospects, Angew. Chemie - Int. Ed. 58 (2019) 15596–15618.

[8] W. Xiang, W. Tress, Review on Recent Progress of All-Inorganic Metal Halide Perovskites and Solar Cells, Adv. Mater. 31 (2019) 1902851.

[9] Q. Ma, S. Huang, X. Wen, M.A. Green, A.W.Y. Ho-Baillie, Hole Transport Layer Free Inorganic CsPbIBr2 Perovskite Solar Cell by Dual Source Thermal Evaporation, Adv. Energy Mater. 6 (2016) 2–6.

[10] J. Lin, M. Lai, L. Dou, C.S. Kley, H. Chen, F. Peng, J. Sun, D. Lu, S.A. Hawks, C. Xie, F. Cui, A.P. Alivisatos, D.T. Limmer, P. Yang, Thermochromic halide perovskite solar cells, Nat. Mater. 17 (2018) 261–267.

[11] V.O. Eze, G.R. Adams, L. Braga Carani, R.J. Simpson, O.I. Okoli, Enhanced Inorganic CsPbIBr2 Perovskite Film for a Sensitive and Rapid Response Self-Powered Photodetector, J. Phys. Chem. C. 124 (2020) 20643–20653.

[12] G.O. Interlayer, Z. Zhang, W. Zhang, Q. Jiang, Z. Wei, Y. Zhang, H.L. You, High-Performance, Vacuum-Free, and Self-Powered CsPbIBr2 Photodetectors Boosted by Ultra-Wide-Bandgap Ga2O3 Interlayer, IEEE Electron Device Lett. 41 (2020) 1532–1535.

[13] Z. Zhang, W. Zhang, Q. Jiang, Z. Wei, M. Deng, D. Chen, W. Zhu, J. Zhang, H. You, Toward High-Performance Electron/Hole-Transporting-Layer-Free, Self-Powered CsPbIBr2 Photodetectors via Interfacial Engineering, ACS Appl. Mater. Interfaces. 12 (2020) 6607–6614.

[14] S.L. Zhang, Ting, Self-Powered All-Inorganic Perovskite Photodetectors with Fast Response Speed, Nanoscale Res. Lett. (2021) 1–13.

[15] Y. Su, X. Chen, W. Ji, Q. Zeng, Z. Ren, Z. Su, L. Liu, Highly Controllable and Efficient Synthesis of Mixed-Halide CsPbX3 (X = Cl, Br, I) Perovskite QDs toward the Tunability of Entire Visible Light, ACS Appl. Mater. Interfaces. 9 (2017) 33020–33028.

[16] W. Zhu, Q. Zhang, D. Chen, Z. Zhang, Z. Lin, J. Chang, J. Zhang, C. Zhang, Y. Hao, Intermolecular Exchange Boosts Efficiency of Air-Stable, Carbon-Based All-Inorganic Planar CsPbIBr2 Perovskite Solar Cells to Over 9%, Adv. Energy Mater. 8 (2018) 1–11.

[17] W.S. Subhani, K. Wang, M. Du, X. Wang, S. (Frank) Liu, Interface-Modification-Induced Gradient Energy Band for Highly Efficient CsPbIBr2 Perovskite Solar Cells, Adv. Energy Mater. 9 (2019) 1–9.

[18] W. Zhu, Z. Zhang, W. Chai, Q. Zhang, D. Chen, Z. Lin, J. Chang, J. Zhang, C. Zhang, Y. Hao, Band Alignment Engineering Towards High Efficiency Carbon-Based Inorganic Planar CsPbIBr2 Perovskite Solar Cells, ChemSusChem. 12 (2019) 2318–2325.

[19] Y. Guo, X. Yin, J. Liu, W. Que, Highly efficient CsPbIBr2 perovskite solar cells with efficiency over 9.8% fabricated using a preheating-assisted spin-coating method, J.

Mater. Chem. A. 7 (2019) 19008–19016.

[20] Y. You, W. Tian, M. Wang, F. Cao, H. Sun, L. Li, PEG Modified CsPbIBr2 Perovskite Film for Efficient and Stable Solar Cells, Adv. Mater. Interfaces. 7 (2020) 1–9.

[21] B. Gao, J. Meng, Highly Stable All-Inorganic CsPbIBr2Perovskite Solar Cells with 11.30% Efficiency Using Crystal Interface Passivation, ACS Appl. Energy Mater. 3 (2020) 8249–8256.

[22] C.F.J. Lau, X. Deng, Q. Ma, J. Zheng, J.S. Yun, M.A. Green, S. Huang, A.W.Y. Ho-Baillie, CsPbIBr2 Perovskite Solar Cell by Spray-Assisted Deposition, ACS Energy Lett. 1 (2016) 573–577.

[23] J. Liang, P. Zhao, C. Wang, Y. Wang, Y. Hu, G. Zhu, L. Ma, J. Liu, Z. Jin, CsPb0.9Sn0.1IBr2 Based All-Inorganic Perovskite Solar Cells with Exceptional Efficiency and Stability, J. Am. Chem. Soc. 139 (2017) 14009–14012.

[24] W. Li, M.U. Rothmann, A. Liu, Z. Wang, Y. Zhang, A.R. Pascoe, J. Lu, L. Jiang, Y. Chen, F. Huang, Y. Peng, Q. Bao, J. Etheridge, U. Bach, Y.-B.B. Cheng, Phase Segregation Enhanced Ion Movement in Efficient Inorganic CsPbIBr2 Solar Cells, Adv. Energy Mater. 7 (2017) 1700946.

[25] Q. Zhang, W. Zhu, D. Chen, Z. Zhang, Z. Lin, J. Chang, J. Zhang, C. Zhang, Y. Hao, Light Processing Enables Efficient Carbon-Based, All-Inorganic Planar CsPbIBr2 Solar Cells with High Photovoltages, ACS Appl. Mater. Interfaces. 11 (2019) 2997–3005.

[26] Y. Peng, T.N. Huq, J. Mei, L. Portilla, R.A. Jagt, L.G. Occhipinti, J.L. MacManus-Driscoll, R.L.Z. Hoye, V. Pecunia, Lead-Free Perovskite-Inspired Absorbers for Indoor Photovoltaics, Adv. Energy Mater. 2002761 (2020) 1–12.

[27] Z. Guo, A.K. Jena, I. Takei, M. Ikegami, A. Ishii, Y. Numata, N. Shibayama, T. Miyasaka, Dopant-Free Polymer HTM-Based CsPbI2Br Solar Cells with Efficiency Over 17 % in Sunlight and 34 % in Indoor Light, Adv. Funct. Mater. 2103614 (2021) 1–9.

[28] B. Parida, I.S. Jin, J.W. Jung, Dual Passivation of SnO2 by Tetramethylammonium Chloride for High-Performance CsPbI2Br-Based Inorganic Perovskite Solar Cells, Chem. Mater. 33 (2021) 5850–5858.

[29] I. Su Jin, K. Su, J. Woong, CsCl-induced defect control of CsPbI2Br thin films for achieving open-circuit voltage of 1.33 V in all-inorganic perovskite solar cells, J. Power Sources. 512 (2021) 230481.

[30] GitHub - mtex-toolbox_mtex_ MTEX is a free Matlab toolbox for quantitative texture analysis, (n.d.). https://github.com/mtex-toolbox/mtex.

[31] N. Fairley, CasaXPS, (2019).

[32] J.J. Zhou, R.Z. Ding, Y.Q. Peng, C.F. Gu, Z.L. Zhou, W.L. Lv, S.N. Xu, L. Sun, Y. Wei, Y. Wang, Light illumination and temperature-induced current–voltage hysteresis in single-crystal perovskite photodiodes, CrystEngComm. 23 (2021) 1663–1670.

[33] B. Yang, M. Wang, X. Hu, T. Zhou, Z. Zang, Highly efficient semitransparent CsPbIBr2 perovskite solar cells via low-temperature processed In2S3 as electron-transport-layer, Nano Energy. 57 (2019) 718–727.

[34] J. Pan, X. Zhang, Y. Zheng, W. Xiang, Morphology control of perovskite film for efficient CsPbIBr2 based inorganic perovskite solar cells, Sol. Energy Mater. Sol. Cells. 221 (2021) 110878.

[35] C. Liu, W. Li, J. Chen, J. Fan, Y. Mai, R.E.I. Schropp, Ultra-thin MoOx as cathode buffer layer for the improvement of all-inorganic CsPbIBr2 perovskite solar cells, Nano Energy. 41 (2017) 75–83.

[36] Y. Guo, F. Zhao, Z. Li, J. Tao, D. Zheng, J. Jiang, J. Chu, Growth control and defect passivation toward efficient and low-temperature processed carbon based CsPbIBr2 solar cell, Org. Electron. 83 (2020) 105731.

[37] B.R. Yongtao Liu, Liam Collins, Roger Proksch, Songkil Kim, Watson, A. V. Doughty, Benjamin, , Tessa R. Calhoun, Mahshid Ahmadi, Ievlev, B.H. and O.S.O. Jesse, Stephen, Scott T. Retterer, Alex Belianinov, Xiao, Kai, Jingsong Huang, Bobby G. Sumpter, Sergei V. Kalinin, Chemical nature of ferroelastic twin domains in CH3NH3PbI3 perovskite, Nat. Mater. 17 (2018) 1013–1019.

[38] S. Jariwala, H. Sun, E.C. Garnett, S. David, S. Jariwala, H. Sun, G.W.P. Adhyaksa, A. Lof, L.A. Muscarella, Local Crystal Misorientation Influences Non- radiative Recombination in Halide Perovskites Local Crystal Misorientation Influences Non-radiative Recombination in Halide Perovskites, Joule. 3 (2019) 3048–3060.

[39] Y. Li, Y. Wang, T. Zhang, S. Yoriya, P. Kumnorkaew, S. Chen, X. Guo, Y. Zhao, Li dopant induces moisture sensitive phase degradation of an all-inorganic CsPbI2Br perovskite, Chem. Commun. 54 (2018) 9809–9812.

[40] Z. Hawash, L.K. Ono, S.R. Raga, M. V. Lee, Y. Qi, Air-exposure induced dopant redistribution and energy level shifts in spin-coated Spiro-Meotad films, Chem. Mater. 27 (2015) 562–569.

[41] E.J. Juárez-Pérez, M.R. Leyden, S. Wang, L.K. Ono, Z. Hawash, Y. Qi, Role of the Dopants on the Morphological and Transport Properties of Spiro-MeOTAD Hole Transport Layer, Chem. Mater. 28 (2016) 5702–5709.

[42] S.A.L. Weber, I.M. Hermes, S.-H. Turren-Cruz, C. Gort, V.W. Bergmann, L. Gilson, A. Hagfeldt, M. Graetzel, W. Tress, R. Diger Berger, How the formation of interfacial charge causes hysteresis in perovskite solar cells, Energy Environ. Sci. 11 (2018) 2404–2413.

[43] H. Sun, G.W.P. Adhyaksa, E.C. Garnett, The Application of Electron Backscatter Diffraction on Halide Perovskite Materials, Adv. Energy Mater. 10 (2020) 2000364.

[44] Z. Zeng, J. Zhang, X. Gan, H. Sun, M. Shang, D. Hou, C. Lu, R. Chen, Y. Zhu, L. Han, In Situ Grain Boundary Functionalization for Stable and Efficient Inorganic CsPbI2Br Perovskite Solar Cells, Adv. Energy Mater. 8 (2018) 1–8.

[45] X. Zheng, Y. Hou, C. Bao, J. Yin, F. Yuan, Z. Huang, K. Song, J. Liu, J. Troughton, N. Gasparini, C. Zhou, Y. Lin, D.J. Xue, B. Chen, A.K. Johnston, N. Wei, M.N. Hedhili, M. Wei, A.Y. Alsalloum, P. Maity, B. Turedi, C. Yang, D. Baran, T.D. Anthopoulos, Y. Han, Z.H. Lu, O.F. Mohammed, F. Gao, E.H. Sargent, O.M. Bakr, Managing grains and interfaces via ligand anchoring enables 22.3%-efficiency inverted perovskite solar cells, Nat. Energy. 5 (2020) 131–140.

[46] J. Zhao, Y. Deng, H. Wei, X. Zheng, Z. Yu, Y. Shao, J.E. Shield, J. Huang, Strained

hybrid perovskite thin films and their impact on the intrinsic stability of perovskite solar cells, Sci. Adv. 3 (2017) 5616. https://doi.org/10.1126/sciadv.aao5616.

[47] R. Lindblad, D. Bi, B. Park, J. Oscarsson, M. Gorgoi, H. Siegbahn, M. Odelius, E.M.J. Johansson, Electronic Structure of TiO2/CH3NH3PbI3 Perovskite Solar Cell Interfaces, J. Phys. Chem. Lett. 4 (2014) 648.

[48] G. Sadoughi, D.E. Starr, E. Handick, S.D. Stranks, M. Gorgoi, R.G. Wilks, M. Baer, H.J. Snaith, Observation and Mediation of the Presence of Metallic Lead in Organic-Inorganic Perovskite Films, ACS Appl. Mater. Interfaces. 7 (2015) 13440–13444.

[49] J.D. Mcgettrick, K. Hooper, A. Pockett, J. Baker, J. Troughton, M. Carnie, T. Watson, Sources of Pb (0) artefacts during XPS analysis of lead halide perovskites, Mater. Lett. 251 (2019) 98–101.

[50] J.K. Nam, M.S. Jung, S.U. Chai, Y.J. Choi, D. Kim, J.H. Park, Unveiling the Crystal Formation of Cesium Lead Mixed-Halide Perovskites for Efficient and Stable Solar Cells, J. Phys. Chem. Lett. 8 (2017) 2936–2940.

[51] C. Liu, W. Li, H. Li, H. Wang, C. Zhang, Y. Yang, X. Gao, Q. Xue, H.L. Yip, J. Fan, R.E.I. Schropp, Y. Mai, Structurally Reconstructed CsPbI2Br Perovskite for Highly Stable and Square-Centimeter All-Inorganic Perovskite Solar Cells, Adv. Energy Mater. 9 (2019) 1803572.

[52] H. Wang, H. Li, S. Cao, M. Wang, J. Chen, Z. Zang, Interface Modulator of Ultrathin Magnesium Oxide for Low-Temperature-Processed Inorganic CsPbIBr2 Perovskite Solar Cells with Efficiency Over 11%, Sol. RRL. 2000226 (2020) 1–11.

[53] S.N. Habisreutinger, T. Leijtens, G.E. Eperon, S.D. Stranks, R.J. Nicholas, H.J. Snaith, Carbon Nanotube/Polymer Composites as a Highly Stable Hole Collection Layer in Perovskite Solar Cells, Nano Lett. 14 (2014) 5561–5568.

[54] J. Liu, S. Pathak, T. Stergiopoulos, T. Leijtens, K. Wojciechowski, S. Schumann, N. Kausch-busies, H.J. Snaith, Employing PEDOT as the p - Type Charge Collection Layer in Regular Organic − Inorganic Perovskite Solar Cells, J. Phys. Chem. Lett. 6 (2015) 1666–1673.

[55] A. Pellaroque, N.K. Noel, S.N. Habisreutinger, Y. Zhang, S. Barlow, S.R. Marder, H.J. Snaith, Efficient and Stable Perovskite Solar Cells Using Molybdenum Tris(dithiolene)s as p-Dopants for Spiro-OMeTAD, ACS Energy Lett. 2 (2017) 2044–2050.

[56] M. Aamir, T. Adhikari, M. Sher, N. Revaprasadu, W. Khalid, J. Akhtar, J.M. Nunzi, Fabrication of planar heterojunction CsPbBr2I perovskite solar cells using ZnO as an electron transport layer and improved solar energy conversion efficiency, New J. Chem. 42 (2018) 14104–14110.

Supplementary information

Crystalline grain engineered $CsPbIBr_2$ films for indoor photovoltaics

Paheli Ghosh[a], Jochen Bruckbauer[b], Carol Trager Cowan[b] and Lethy Krishnan Jagadamma[a*]

[a]Energy Harvesting Research Group, School of Physics & Astronomy, SUPA, University of St Andrews, St Andrews, KY16 9SS, United Kingdom

[b]Department of Physics, SUPA, University of Strathclyde, Glasgow, G4 0NG, United Kingdom

Email: lkj2@st-andrews.ac.uk

Photovoltaic properties

Table S1 Photovoltaic parameters of $CsPbIBr_2$ based devices under different indoor lamps (34 devices were measured under daylight white LED, 12 devices under cool white LED, 8 devices under CFL and 10 devices under warm white LED).

Lamps	Direction of scan	J_{SC} (mA cm^{-2})	V_{OC} (V)	FF (%)	PCE $_{Avg}$ (%)	PCE $_{max}$ (%)	Power input (mW cm^{-2})	Power outpout (μW cm^{-2})
Daylight white LED	Forward	0.05±0.01	0.71±0.12	39.56±4.71	6.0±2.2	9.1	0.25	14.9±5.4
	Reverse	0.05±0.01	0.75±0.15	55.11±6.04	8.5±2.9	14.1		21.1±7.3
Cool white LED	Forward	0.03±0.01	0.61±0.1	38.63±6.66	3.1±1.6	6.0	0.25	7.86±4.0
	Reverse	0.04±0.01	0.64±0.1	55.77±3.47	5.3±1.9	9.4		13.4±4.8
CFL	Forward	0.04±0.02	0.56±0.09	39.48±5.19	3.4±1.9	7.0	0.25	8.6±4.3
	Reverse	0.04±0.01	0.64±0.12	53.01±5.4	5.6±1.5	8.7		14.1±3.7

Warm white LED	Forward	0.03±0.01	0.56±0.09	36.78±6.58	2.0±0.8	3.8	0.30	5.9±2.5
	Reverse	0.03±0.01	0.58±0.13	53.88±4.19	3.2±1.3	6.3		9.5±4.0

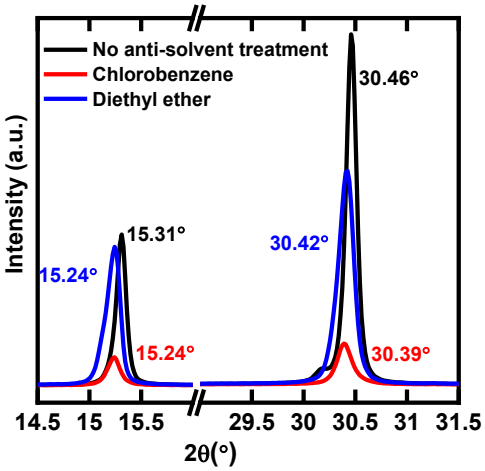

Figure S1 X-ray diffractograms of the $CsPbIBr_2$ films without any anti-solvent, and with chlorobenzene and diethyl ether treatment showing the *inferior crystal quality after chlorobenzene treatment* displacement of the XRD peaks around 15.2° and 30.4° due to the treatment with different anti-solvents.

Table S2 Comparison of the device performance of $CsPbIBr_2$ devices fabricated without anti-solvent treatment (26 photovoltaic devices), with chlorobenzene (12 devices) and diethyl ether (50 devices) under 1 Sun condition.

Anti-solvent	**Direction of scan**	**J_{SC} (mAcm^{-2})**	**V_{OC} (V)**	**FF (%)**	**PCE_{Avg} (%)**	**PCE_{max} (%)**
No anti-solvent	Forward	6.60±1.10	0.99±0.09	47.4±3.23	3.1±0.7	4.4
	Reverse	6.20±0.92	0.99±0.09	61.69±4.79	3.9±1.0	5.9
Chlorobenzene	Forward	4.82±0.54	0.83±0.13	50.58±9.05	2.0±0.3	2.2
	Reverse	4.81±0.27	0.92±0.04	61.47±2.21	2.7±0.3	3.0
Diethyl ether	Forward	7.48±0.81	1.03±0.07	47.92±4.29	3.7±0.7	5.3
	Reverse	6.72±0.99	1.01±0.05	66.82±5.85	4.5±0.6	5.9

The average J_{SC} recorded for devices without anti-solvent treatment was 6.6±1.1 mA cm^{-2} and 6.2±0.9 mA cm^{-2} in forward and reverse scans, respectively, which were significantly lower compared to the average performance of devices with diethyl ether treatment, 7.48±0.81 mA cm^{-2} and 6.72±0.99 mA cm^{-2} in forward and reverse scans, respectively. Devices fabricated using chlorobenzene treatment showed the lowest average J_{SC} of 4.82±0.54 mA cm^{-2} and 4.81±0.27 mA cm^{-2} in forward and reverse scans, respectively. The devices with diethyl ether treated perovskite films recorded a higher average V_{OC} (1.03±0.07 V and 1.01±0.05 V in forward and reverse scan, respectively) compared to devices without anti-solvent treatment (0.99±0.09 V in both forward and reverse scans). However, the forward scan FF showed marginal improvement with diethyl ether treatment (47.92±4.29%) as compared to films without anti-solvent treatment (47.4±3.2%) whereas reverse scans showed a substantial increase in FF from 61.7±4.8% for devices without any anti-solvent to 66.82±5.85% for diethyl ether treated devices.

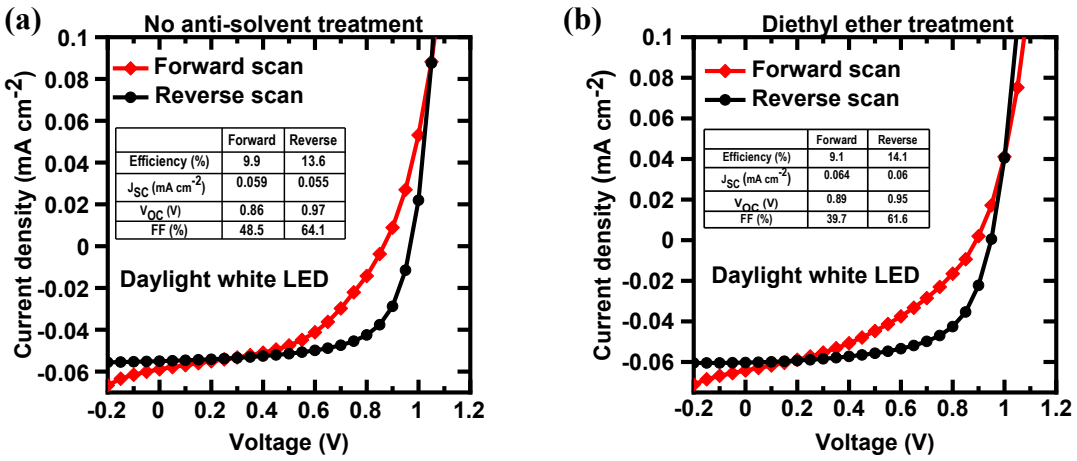

Figure S2 Current density *versus* voltage curves for the best performing device with (a) no anti-solvent treatment and (b) diethyl ether treatment in forward and reverse scans along with the photovoltaic parameters under daylight white LED light.

Under daylight white LED illumination, the devices fabricated without any anti-solvent treatment recorded the best PCE of 9.9% and 13.6% during forward and reverse scans, respectively, with the average photovoltaic parameters recorded as 0.05±0.01 mA cm^{-2}, 0.77±0.16 V and 53.86±7.76% in the reverse scan [Figure S2 and Table S3]. Though diethyl

ether treatment showed similar average J_{SC} and V_{OC} values, the FF showed slight improvement to 55.1±6.04% in reverse scan with a champion PCE of 14.1%.

Table S3 Comparison of the device performance of $CsPbIBr_2$ devices fabricated without anti-solvent (17 photovoltaic devices) and with diethyl ether treatment (36 devices under indoor daylight white LED light).

Anti-solvent	Direction of scan	J_{SC} (mAcm^{-2})	V_{OC} (V)	FF (%)	PCE $_{Avg}$ (%)	PCE $_{max}$ (%)	Power input (mW cm^{-2})	Power output $_{Avg}$ (µW cm^{-2})
No anti-solvent	Forward	0.05±0.01	0.7±0.16	38.32±5.47	5.7±2.8	9.9	0.25	14.1±7.1
	Reverse	0.05±0.01	0.77±0.16	53.86±7.76	8.36±3.5	13.6		20.5±8.9
Chlorobenzene	Forward	Measurements under indoor illumination not undertaken since the photovoltaic parameters recorded under 1 Sun condition were poor compared to devices without anti-solvent and diethyl ether treatment and devices lacked air-stability						
	Reverse							
Diethyl ether	Forward	0.05±0.01	0.71±0.12	39.56±4.71	6.0±2.2	9.1	0.25	14.9±5.4
	Reverse	0.05±0.01	0.75±0.15	55.11±6.04	8.5±2.9	14.1		21.1±7.3
DEE 500 uL	FW	0.042±0.01	0.51±0.09	38.28±9.99	3.16±0.96	5.68	0.25	7.9±2.4
	RW	0.042±0.01	0.45±0.13	46.49±9.07	3.68±1.85	9.18	0.25	9.2±4.6

Optimisation of device performance with different volume of diethyl ether

The best device performance under both 1 Sun and daylight white LED illumination was obtained using devices with diethyl ether treatment, hence, this section is dedicated to the optimisation of the volume of diethyl ether required for the anti-solvent treatment. Different volumes of diethyl ether, 100, 250, 500 and 750 µL, were used for the anti-solvent treatment process. The corresponding J-V characteristics of the devices are shown in Figure S3. The maximum PCE for devices treated with 100 µL diethyl ether were recorded as 3.8% and 3.1% in forward and reverse scans, respectively. When the volume was increased to 250 µL, the maximum PCE increased to 4.5% in reverse scan whereas a slight drop (0.4%) was noted during the forward scan. Increasing the volume further to 500 µL resulted in the best PCE of 4.5% in forward and 5.6% in the reverse scan. However, the hysteresis index was very high (20%). *Treatment using 750 µL diethyl ether resulted in a slight increase in the maximum PCE during the forward scan but there was no significant variation in the reverse scan with the optimised PCE of 5.9% as reported in the main text. Moreover, the average photovoltaic parameters also became almost steady after 500 and 750 µL of diethyl ether treatment [Table S4]. Since the device performance was saturated after treatment with 500 and 750 µL diethyl ether recording similar photovoltaic parameters, the effect of larger volumes of anti-solvent was not explored.* The optimised volume for device fabrication was determined as 750 µL, since it not only resulted in good device performance with repeatability and very low hysteresis index but also recorded the highest J_{SC} and FF with one of the best V_{OC}. Moreover, devices using low volumes (100, 250 and 500 µL) of diethyl ether rapidly degraded during 1 Sun measurement with the $CsPbIBr_2$ perovskite film undergoing discolouration into the yellow non-perovskite phase as shown in Figure S4. The photovoltaic parameters recorded for devices fabricated using different volume of diethyl ether treatment are summarized in Table S4. Figure S4 shows the photographs of the degraded devices with low volume of diethyl ether as observed from (a) Au side and (b) Glass/ITO side (A1/A2 - 100 µL, B1/B2 - 250 µL, C1/C2 - 500 µL and SW-2 - 750 µL).

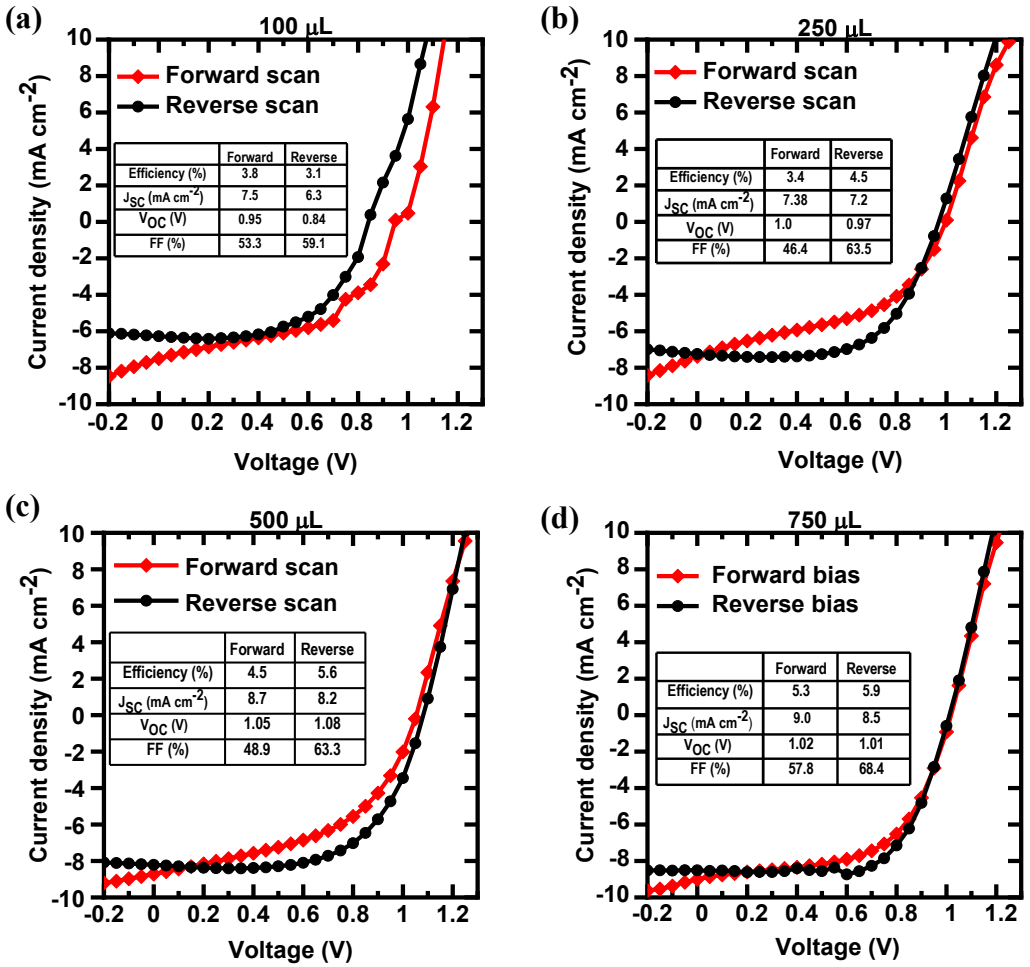

Figure S3 Current density *versus* voltage curves for the best performing devices with different volumes (a) 100 µL, (b) 250 µL, (c) 500 µL and (d) 750 µL of diethyl ether anti-solvent along with the photovoltaic parameters in forward and reverse scans under 1 Sun.

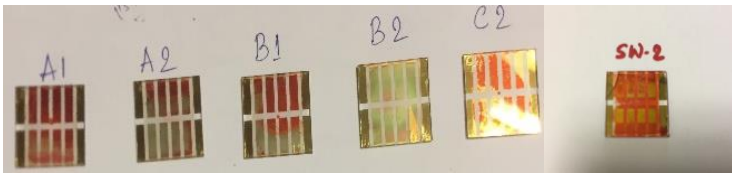

Figure S4 Degradation of the devices with low volume of diethyl ether as observed from glass/ITO side (A1/A2 – 100 µL, B1/B2 – 250 µL, C1/C2 – 500 µL and SW-2 – 750 µL) (RH ~33%).

Table S4 Comparison of the device performance of $CsPbIBr_2$ devices under 1 Sun condition fabricated using different volumes (100, 250, 500 and 750 µL) of diethyl ether. For 100, 250 and 500 µL samples, 14, 7 and 10 photovoltaic devices, respectively, were considered whereas 50 devices were averaged for the 750 µL optimised volume samples.

Volume of diethyl ether (µL)	Direction of scan	J_{SC} (mAcm^{-2})	V_{OC} (V)	FF (%)	PCE_{Avg} (%)	PCE_{max} (%)
100	Forward	5.40±1.63	0.88±0.21	50.92±5.86	2.4±0.9	3.8
	Reverse	4.47±1.39	0.85±0.03	67.92±6.69	2.5±0.6	3.1
250	Forward	5.05±2.22	0.96±0.05	47.12±3.42	2.3±1.3	4.4
	Reverse	4.30±2.11	0.83±0.14	69.37±6.8	2.5±1.2	4.5
500	Forward	6.70±1.25	0.97±0.07	48.27±4.44	3.2±0.8	4.5
	Reverse	6.22±1.2	0.96±0.08	62.57±3.92	3.8±1.0	5.6
750	Forward	7.48±0.81	1.03±0.07	47.92±4.29	3.7±0.7	5.3
	Reverse	6.72±0.99	1.01±0.05	66.82±5.85	4.5±0.6	5.9

Electron backscatter diffraction (EBSD) characterisation

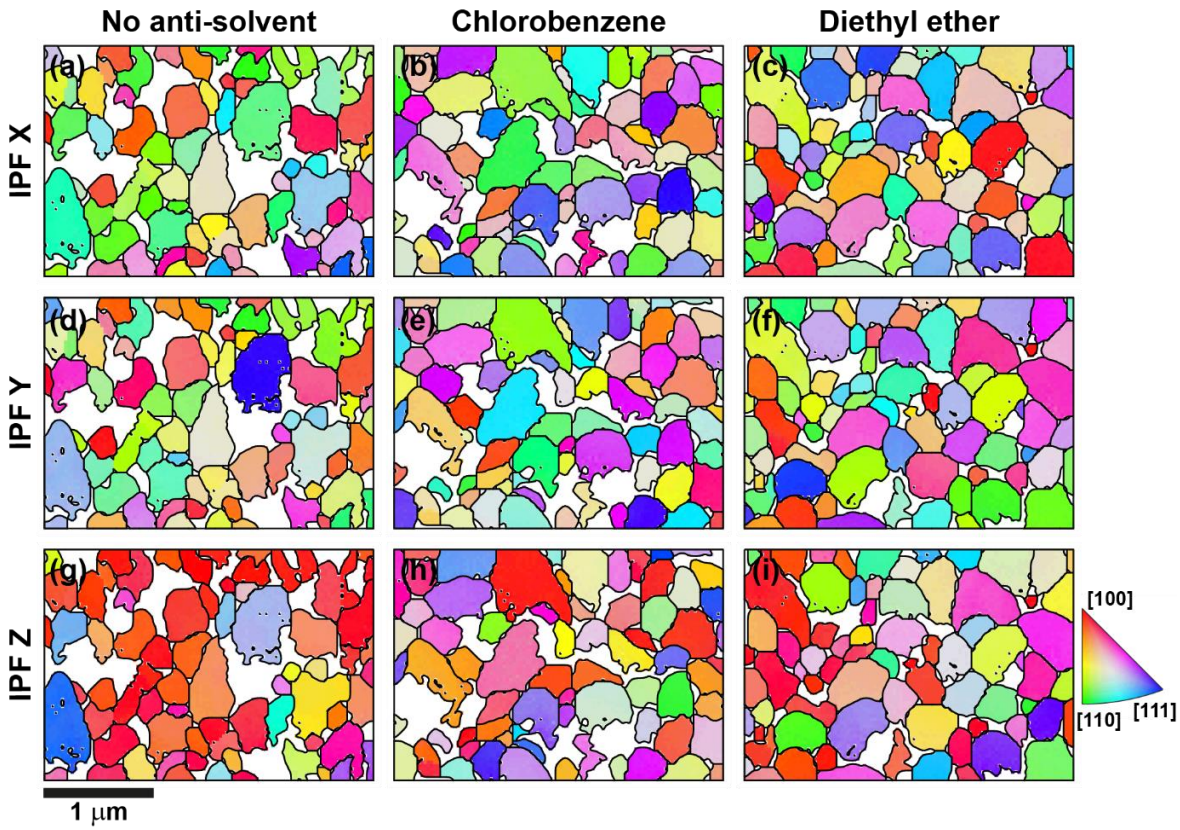

Figure S5 IPF X, Y and Z maps for the three $CsPbIBr_2$ films, without anti-solvent treatment (first column), with chlorobenzene (second column) and diethyl ether (third column) treatment. The colour key at the bottom right applies to all maps.

Figure S5 shows the inverse pole figure (IPF) maps for the sample X, Y and Z directions for the three $CsPbIBr_2$ films without anti-solvent treatment, with chlorobenzene and diethyl ether treatment. **Figure S6** shows the pole figures for the (100) plane for the three $CsPbIBr_2$ films with individually adjusted colour scales.

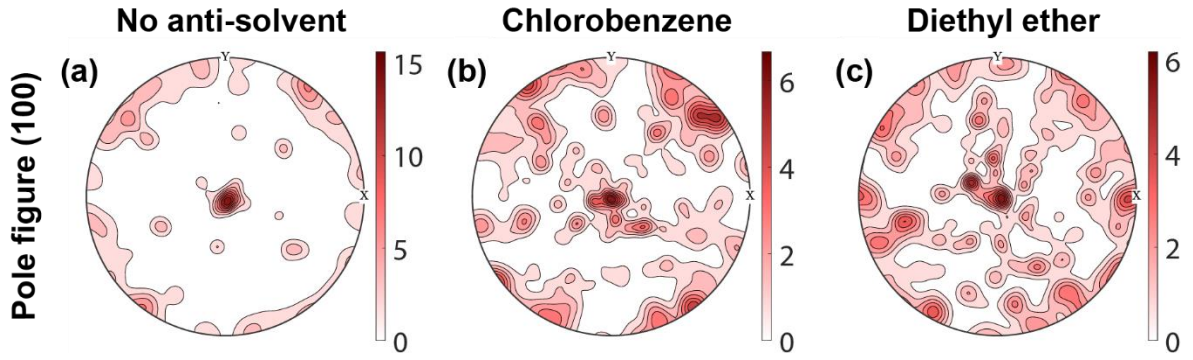

Figure S6 Pole figure for the (100) plane for the three $CsPbIBr_2$ films, (a) without anti-solvent treatment, (b) with chlorobenzene and (c) diethyl ether treatment.

Table S5 Mean area, mean perimeter, and mean circle equivalent diameter and mean GOS estimated from the EBSD results.

	No Anti-solvent	**Chlorobenzene**	**Diethyl ether**
Mean area (μm^2)	0.08±0.01	0.08±0.01	0.08±0.01
Mean perimeter (μm)	1.16±0.11	1.10±0.08	1.05±0.07
Mean circle equivalent diameter (μm)	0.30±0.02	0.29±0.02	0.29±0.02
Mean GOS (˚)	0.68±0.18	0.47±0.06	0.39±0.03

X-ray photoelectron spectroscopy (XPS) characterisation

Figure S7 shows the wide scan of the $CsPbIBr_2$ films prepared without anti-solvent treatment, with chlorobenzene and diethyl ether treatment. Clear signature peaks of Cs, Pb, I, and Br are detected with a negligible amount of carbon in the form of adventitious carbon which is commonly expected in any *ex-situ* prepared sample. The lack of any other impurity peak can be regarded as an indicator of the compositional purity of the $CsPbIBr_2$ films.

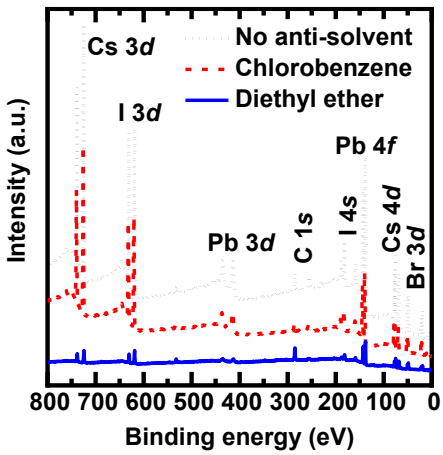

Figure S7 XPS wide scan of $CsPbIBr_2$ films without anti-solvent, with chlorobenzene, and diethyl ether treatment.

X-ray diffraction of aged $CsPbIBr_2$ film and Glass/ITO/SnO_2/$CsPbIBr_2$/Spiro-OMeTAD/Au device stack

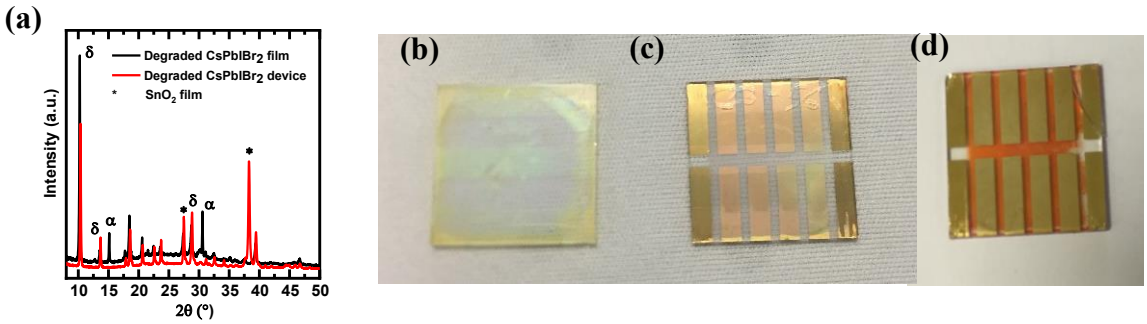

Figure S8 (a) The X-ray diffraction patterns of the aged $CsPbIBr_2$ film (black line - XRD intensity signal has been multiplied by 2) and Glass/ITO/SnO_2/$CsPbIBr_2$/Spiro-OMeTAD/Au device stack (red line). (b & c) Photographs of the (b) aged degraded $CsPbIBr_2$ film and (c) Glass/ITO/SnO_2/$CsPbIBr_2$/Spiro-OMeTAD/Au device stack. (d) Photograph of the freshly prepared photovoltaic device is shown to highlight the contrast in colour between the perovskite and the non-perovskite phase.

The X-ray diffraction patterns of the air-aged $CsPbIBr_2$ film and Glass/ITO/SnO_2/$CsPbIBr_2$/Spiro-OMeTAD/Au device stack are shown in Figure S8. The

presence of the peak at 10.24° can be assigned to the δ-phase of $CsPbIBr_2$ [1–5]. This peak is visible in both the $CsPbIBr_2$ film and the $CsPbIBr_2$ based device stack clearly demonstrating that the as-deposited α-phase of the $CsPbIBr_2$ perovskite has degraded into the yellow non-perovskite orthorhombic δ-phase after ageing in air. Interestingly, the $CsPbIBr_2$ film still shows the presence of the (100) and (200) planes of the cubic α-phase at 15.2° and 30.4°, respectively, whereas no such peak is observed in case of the aged device stack which highlights the complete degradation of the device in the presence of hygroscopic Li-TFSI dopant used in Spiro-OMeTAD hole conductor which in turn facilitates moisture ingress into the perovskite layer. Photographs of the aged and degraded $CsPbIBr_2$ film and the Glass/ITO/SnO_2/$CsPbIBr_2$/Spiro-OMeTAD/Au device stack are shown in Figure S8 (b) and (c), respectively. Photograph of the freshly prepared photovoltaic device is shown in Figure S8 (d) to highlight the contrast in colour between the perovskite and the non-perovskite phase.

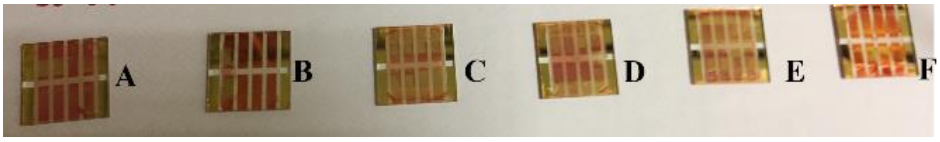

Figure S9 Photographs of the degradation of the devices without and with different anti-solvents as observed from the Glass/ITO side (A/B - without anti-solvent treatment, C/D - with chlorobenzene treatment, and E/F – with diethyl ether treatment) (RH ~ 33%).

FTIR Spectra of the $CsPbIBr_2$ heterostructures

Figure S10 (a) shows the FTIR spectra of freshly prepared doped Spiro-OMeTAD films (black line) deposited on ITO substrate and the same film aged in air for 3-4 hours (red line). In the freshly prepared Spiro-OMeTAD films, absorption peaks are seen in the range of 3100-2800 cm^{-1}, 2400-2200 cm^{-1}, and 1500-700 cm^{-1}. The peaks in the range of 3100-2800 cm^{-1} can be associated with C-H stretches (both aromatic and non-aromatic) whereas the bands in the region of 2400-2200 cm^{-1} can be attributed to R-C-N vibrations arising mainly from the FK 209 dopant molecules. The absorption intensity of the C-H vibrations is reduced for the Spiro-OMeTAD films after ageing in air. The intensity of absorption bands in the FTIR spectra depends on two factors (a) the change in dipole moment with distance and (b) the concentration of molecules. Here, the reduced intensity of C-H vibrations for the aged Spiro-OMeTAD films implies that either the change in dipole moment with distance for this vibration is lower than

that of freshly prepared Spiro-OMeTAD films or the concentration of the molecule is reduced corresponding to this vibration. Since the C-H vibration can arise from Spiro-OMeTAD as well as from the dopant molecule, assigning this to a particular molecule is difficult as previously noted [6]. The R-C-N band was not observed in the previously reported FTIR spectra of Spiro-OMeTAD films doped with Li-TFSI and tBP. The peaks at 2376 and 2319 cm^{-1} for the fresh Spiro-OMeTAD films shifts to 2361 and 2332 cm^{-1} for the aged Spiro-OMeTAD films. These shifts in wavenumbers can be attributed to the change in bond length. Based on previous reports of FTIR on undoped Spiro-OMeTAD by Hawash *et al.* [6] and Perez *et al*. [7], the absorption peak at 1506 cm^{-1} and 1450 cm^{-1} are associated with C=C stretches, and vibration mode at 1240 cm^{-1} corresponds to a stretch consistent with C-N bonds. In addition to these, the absorption peaks are seen at 1036 cm^{-1}, 827 and 736 cm^{-1} which can be attributed to in-plane (1036 cm^{-1}) and out of plane (736 cm^{-1}) C-H bending modes. Comparing the FTIR spectra of freshly prepared Spiro-OMeTAD films and the aged films shows the following main differences, (a) a new absorption peak at 1607 cm^{-1} appears for aged Spiro-OMeTAD films which was absent in the freshly prepared Spiro films. This vibration mode can be assigned to aromatic C-C stretching. (b) The relative absorption intensity of the peaks at 1503 and 1240 cm^{-1} is reduced for the Spiro-OMeTAD films aged in air. The reduction in intensity corresponding to this C=C vibrations can result from the distortion in the conjugation structure in Spiro-OMeTAD due to air exposure.

Figure S10 (b) shows the comparison of the FTIR spectra of freshly prepared Spiro-OMeTAD on the $CsPbIBr_2$ films. These spectra are quite similar to that of freshly prepared Spiro-OMeTAD films on the ITO substrate. Crystal structure analysis shows that $CsPbIBr_2$ films are cubic and hence, no FTIR signal is expected from the $CsPbIBr_2$. **Figure S10 (c)** shows the comparison of the air-aged Spiro-OMeTAD films on the $CsPbIBr_2$ films. Spiro-OMeTAD films deposited on the chlorobenzene and diethyl ether anti-solvent treated $CsPbIBr_2$ perovskite layer show a similar spectral appearance to that of freshly prepared Spiro-OMeTAD even after 3 hours of air exposure. However, the Spiro-OMeTAD films deposited on the $CsPbIBr_2$ films without any anti-solvent treatment show a similar spectral shape of Spiro-OMeTAD with reduced relative intensity for C=C peaks at 1503 and 1240 cm^{-1}, which can be attributed to the structural deformation or degradation of the Spiro-OMeTAD molecule.

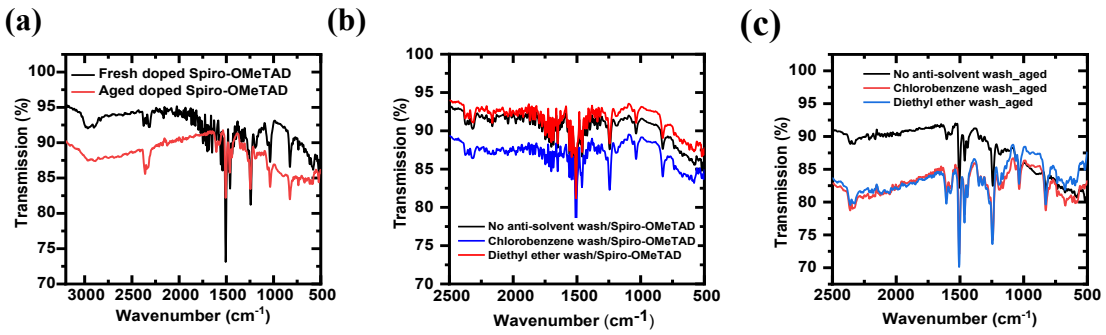

Figure S10 (a) FTIR spectra comparison of freshly prepared and air-aged Spiro-OMeTAD films on ITO substrate. (b) Comparison of the FTIR spectra of freshly prepared Spiro-OMeTAD films on the $CsPbIBr_2$ perovskite layers fabricated without anti-solvent and with chlorobenzene and diethyl ether treatment. (c) Comparison of the FTIR spectra of air-aged Spiro-OMeTAD films on the $CsPbIBr_2$ films fabricated using different treatment conditions.

Powering the sensor circuit

To verify their applicability for indoor and outdoor Internet of Things (IoT) applications, the devices were used for powering a non-inverting buffer with open-drain output [74AUP1G07] to implement a single input logic gate. Low-power electronic components such as digital buffers can function as an important component of the IoT applications as they can isolate logic gates, (especially when there is impedance mismatch) and for power amplification. A non-inverting buffer produces an output that exactly matches its input. The input and output voltage transfer curves under three different powering conditions are shown in **Figure S10**. The input square signal is supplied by a function generator (Tektronix; Model TBS 1052B-EDU), with specifications of 1 kHz frequency, 1.5 V (Vpp) and 50% duty cycle. When the buffer circuit is powered by the 1.5 V (AA) battery, the output voltage signal is identical to that of the input signal with an output voltage of 1.4 V. On replacing the battery with a solar cell illuminated under 1 Sun, the output voltage shape is retained but the voltage dropped to 0.65 V. Under indoor lighting spectra with daylight white LED with an irradiance of 0.25 mW cm^{-2} (illuminance of 1000 lux), even though the digital buffer circuit is turned on, the output voltage shape is not retained and an output voltage of only ~0.125 V is obtained. The lower current in microamperes under indoor illumination will be the limiting factor for the reduced output voltage from the buffer circuit.

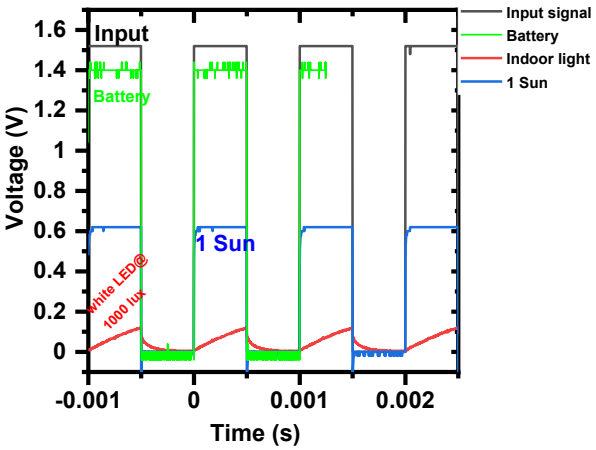

Figure S11 Output transients of buffer circuit which were powered using battery and the Glass/ITO/SnO_2/$CsPbIBr_2$/Spiro-OMeTAD/Au device stack under different illumination.

References

[1] J. Lin, M. Lai, L. Dou, C.S. Kley, H. Chen, F. Peng, J. Sun, D. Lu, S.A. Hawks, C. Xie, F. Cui, A.P. Alivisatos, D.T. Limmer, P. Yang, Thermochromic halide perovskite solar cells, Nat. Mater. 17 (2018) 261–267.

[2] Y. Guo, F. Zhao, Z. Li, J. Tao, D. Zheng, J. Jiang, J. Chu, Growth control and defect passivation toward efficient and low-temperature processed carbon based CsPbIBr2 solar cell, Org. Electron. 83 (2020) 105731.

[3] J.K. Nam, M.S. Jung, S.U. Chai, Y.J. Choi, D. Kim, J.H. Park, Unveiling the Crystal Formation of Cesium Lead Mixed-Halide Perovskites for Efficient and Stable Solar Cells, J. Phys. Chem. Lett. 8 (2017) 2936–2940.

[4] C. Liu, W. Li, H. Li, H. Wang, C. Zhang, Y. Yang, X. Gao, Q. Xue, H.L. Yip, J. Fan, R.E.I. Schropp, Y. Mai, Structurally Reconstructed CsPbI2Br Perovskite for Highly Stable and Square-Centimeter All-Inorganic Perovskite Solar Cells, Adv. Energy Mater. 9 (2019) 1803572.

[5] H. Wang, H. Li, S. Cao, M. Wang, J. Chen, Z. Zang, Interface Modulator of Ultrathin Magnesium Oxide for Low-Temperature-Processed Inorganic CsPbIBr2 Perovskite Solar Cells with Efficiency Over 11%, Sol. RRL. 2000226 (2020) 1–11.

[6] Z. Hawash, L.K. Ono, S.R. Raga, M. V. Lee, Y. Qi, Air-exposure induced dopant redistribution and energy level shifts in spin-coated Spiro-Meotad films, Chem. Mater. 27 (2015) 562–569.

[7] E.J. Juárez-Pérez, M.R. Leyden, S. Wang, L.K. Ono, Z. Hawash, Y. Qi, Role of the Dopants on the Morphological and Transport Properties of Spiro-MeOTAD Hole Transport Layer, Chem. Mater. 28 (2016) 5702–5709.